






# Three-dimensional Features of the Outer Heliosphere Due to Coupling between the Interstellar and Heliospheric Magnetic Field. V. The Bow Wave, Heliospheric Boundary Layer, Instabilities, and Magnetic Reconnection

N. V. Pogorelov<sup>1,2</sup> , J. Heerikhuisen<sup>1,2</sup>, V. Roytershteyn<sup>3</sup>, L. F. Burlaga<sup>4</sup> , D. A. Gurnett<sup>5</sup> , and W. S. Kurth<sup>5</sup>

<sup>1</sup>Department of Space Science, The University of Alabama in Huntsville, AL 35805, USA; [nikolai.pogorelov@uah.edu](mailto:nikolai.pogorelov@uah.edu)

<sup>2</sup>Center for Space Plasma and Aeronomic Research, The University of Alabama in Huntsville, AL 35805, USA

<sup>3</sup>Space Science Institute, Boulder, CO 80301, USA

<sup>4</sup>NASA Goddard Space Flight Center, Greenbelt, MD 20771, USA

<sup>5</sup>Department of Physics and Astronomy, The University of Iowa, Iowa City, IA 52242, USA

Received 2017 May 1; revised 2017 June 24; accepted 2017 June 27; published 2017 August 4

## Abstract

The heliosphere is formed due to interaction between the solar wind (SW) and local interstellar medium (LISM). The shape and position of the heliospheric boundary, the heliopause, in space depend on the parameters of interacting plasma flows. The interplay between the asymmetrizing effect of the interstellar magnetic field and charge exchange between ions and neutral atoms plays an important role in the SW–LISM interaction. By performing three-dimensional, MHD plasma/kinetic neutral atom simulations, we determine the width of the outer heliosheath—the LISM plasma region affected by the presence of the heliosphere—and analyze quantitatively the distributions in front of the heliopause. It is shown that charge exchange modifies the LISM plasma to such extent that the contribution of a shock transition to the total variation of plasma parameters becomes small even if the LISM velocity exceeds the fast magnetosonic speed in the unperturbed medium. By performing adaptive mesh refinement simulations, we show that a distinct boundary layer of decreased plasma density and enhanced magnetic field should be observed on the interstellar side of the heliopause. We show that this behavior is in agreement with the plasma oscillations of increasing frequency observed by the plasma wave instrument onboard *Voyager 1*. We also demonstrate that *Voyager* observations in the inner heliosheath between the heliospheric termination shock and the heliopause are consistent with dissipation of the heliospheric magnetic field. The choice of LISM parameters in this analysis is based on the simulations that fit observations of energetic neutral atoms performed by *Interstellar Boundary Explorer*.

**Key words:** ISM: kinematics and dynamics – magnetic fields – solar wind – Sun: heliosphere

**Supporting material:** animations

## 1. Introduction

The interaction of the solar wind (SW) with the local interstellar medium (LISM) is essentially the combination of a blunt-body and a supersonic jet flows. Head-on collision of the SW and LISM plasma flows creates a tangential discontinuity (the heliopause, HP), which extends far into the wake region (see Figure 1). The SW flow in the direction parallel to the Sun’s motion resembles a jet immersed into a medium with lower thermal pressure. The LISM plasma is decelerated at the HP, which may result, depending on the LISM parameters, in the formation of a so-called bow shock (BS). The SW flow, on the other hand, is decelerated due to its interaction with the HP, charge exchange with interstellar neutral atoms, and by the LISM counter-pressure in the heliotail region. Since the neutral hydrogen (H) density in the LISM is greater than the proton density, resonant charge exchange between ions and neutral ions plays a major role in the SW–LISM interactions (Blum & Fahr 1969; Wallis 1971, 1975; Holzer 1977). In particular, the SW in the tail is decelerated and cooled down by charge exchange until the heliotail disappears at a few tens of thousands of au (Izmodenov & Alexashov 2003). Because of the large mean free path, charge exchange and, in general, the transport of neutral atoms should be performed kinetically, by solving the Boltzmann equation. The first self-consistent simulation of this kind was performed by Baranov & Malama (1993) in an axially symmetric statement of the problem neglecting the effect of the

heliospheric and interstellar magnetic fields (HMF and ISMF). This model was extended to time-dependent (Izmodenov et al. 2005b) and 3D flows (Izmodenov et al. 2005a) much later. Another class of models assume that neutral atoms can be treated as a fluid, or rather a set of fluids, each of them describing the flow of neutral atoms born in thermodynamically different regions of the SW–LISM interaction. These are usually (i) the unperturbed LISM; (ii) the LISM region substantially modified by the presence of the heliosphere; (iii) the region between the TS and HP; and (iv) the supersonic SW region (Pauls et al. 1995; Zank et al. 1996; Fahr et al. 2000; Florinski et al. 2004; Pogorelov et al. 2006). Such multi-fluid approaches are easily applicable to genuinely time-dependent problems (see, e.g., Zank & Müller 2003; Sternal et al. 2008; Pogorelov et al. 2009a, 2013a, 2013c), which are very expensive computationally when neutrals atoms are treated kinetically (Izmodenov et al. 2005b; Zirnstein et al. 2015b).

Figure 1 shows a typical simulation result that takes into account solar cycle effects. The inner boundary conditions, corresponding to a nominal solar cycle with the radial velocity, ion density, and temperature in the fast and slow SW, are specified at the Earth orbit ( $R = 1$  au). It is assumed that the latitudinal extent of the slow wind varies with an 11-year period from  $\theta = 28^\circ$  at solar minima to  $90^\circ$  at solar maxima. In addition, the tilt between the Sun’s magnetic and rotation axes varies from  $\theta = 8^\circ$  at solar minima to  $90^\circ$  at solar maxima and

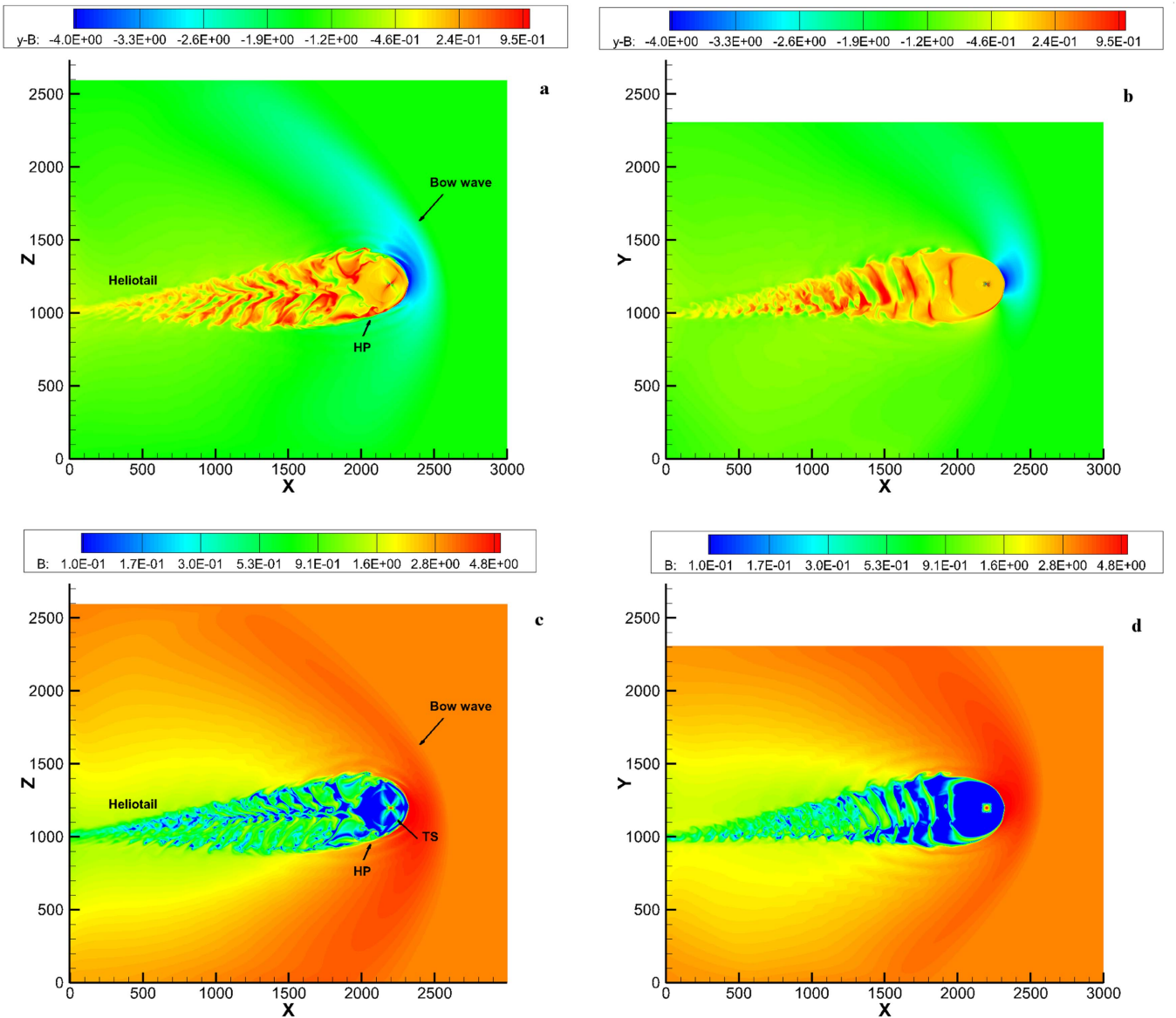


**Figure 1.** SW–LISM interaction pattern in the presence of solar cycle effects. The  $y$ -component (top panels) of the magnetic field vector and its magnitude (bottom panels) in the meridional (left panels) and equatorial (right panels) planes. Distances are given in au and magnetic field in  $\mu\text{G}$ . One can see the TS, HP, and bow wave.

flips to the opposite hemisphere at each maximum. This creates a sequence of regions possessing opposite HMF polarities in the heliotail. We perform all simulations in a so-called heliospheric coordinate system, where the  $z$ -axis is aligned with the Sun’s rotation axis, the  $x$ -axis belongs to the plane formed by the  $z$ -axis and  $\mathbf{V}_\infty$ , and is directed upstream into the LISM. The  $y$ -axis completes the right coordinate system. The boundary conditions in the SW and LISM are taken from the existing simulation (Borovikov & Pogorelov 2014) and are for illustration purposes only. In summary, the heliosphere is characterized by the presence of a very long heliotail, which extends to distances exceeding 5000 au, and is compressed approximately in the direction perpendicular to the  $BV$ -plane. The latter is defined by the LISM velocity and ISMF vectors,  $\mathbf{V}_\infty$  and  $\mathbf{B}_\infty$ , in the unperturbed LISM. The width of the heliotail in the plane of its maximum flaring (the  $BV$ -plane) decreases with distance from the Sun. This creates an illusion that the heliotail disappears when we look at the mutually perpendicular cross-sections shown in Figure 1. Three-dimensional

pictures of the heliosphere can be found in Borovikov & Pogorelov (2014). We will discuss the boundary conditions in the LISM in Section 3.

In principle, some sort of kinetic treatment of neutral atoms is preferred because the charge exchange mean free path is about 50–100 au, depending on the region of the heliosphere and the origin of H atoms. This is especially important for simulations aimed to provide input to calculations of energetic neutral atoms (ENAs) observed by the *Interstellar Boundary Explorer* (IBEX); see McComas et al. (2017) for a review of the mission results over the past 7 years. In particular, the secondary H atoms born in the SW are of importance if we are interested in the distance to which the heliosphere may affect the LISM flow. It is known from theory and simulations (Gruntman 1982; Baranov & Malama 1993; Zank et al. 1996) that secondary neutral atoms can travel far upwind where they may experience charge exchange and affect the LISM flow. A number of the IBEX ribbon models (Chalov et al. 2010; Heerikhuisen et al. 2010; Isenberg 2014; Giacalone &

Jokipii 2015) involve secondary neutral atoms. Radio emission in a 2–3 kHz range observed by *VI* also relies upon global shock waves propagating outward due to various solar events and “the neutral SW” (H atoms born inside the TS) as a source of pickup ions (PUIs) that initiate a series of physical processes which ultimately result in the observed wave activity (Gurnett et al. 1993, 2006, 2013, 2015; Cairns & Zank 2002; Pogorelov et al. 2008, 2009b; Mitchell et al. 2009). It is believed that the ring-beam instability of PUIs born in the outer heliosheath (OHS; i.e., in the region of the LISM affected by the presence of the heliosphere) resonantly accelerates ambient electrons by lower hybrid waves. These pre-accelerated electrons are further accelerated by transient shocks creating the foreshock electron beams, plasma waves, and radio emission. Secondary neutral atoms are also important to establish the geometrical size the OHS. The speed and temperature of the unperturbed LISM can be derived from the properties of He atoms observed by such Earth-bound spacecraft as *Ulysses* and *IBEX* (Witte 2004; Bzowski et al. 2015; McComas et al. 2015). It was shown that the pristine LISM flow is supersonic, and one would expect a bow shock to be formed in front of the HP. However, the LISM is magnetized, so its flow may become subfast magnetosonic (its speed being less than the fast magnetosonic speed), which will eliminate the fast-mode bow shock. In principle, slow-mode shocks may still exist in front of the HP (Florinski et al. 2004; Pogorelov et al. 2006, 2011; Zieger et al. 2013) if the angle between  $V_\infty$  and  $B_\infty$  is small. In this paper, we will show that this is an unlikely scenario in the presence of charge exchange of LISM ions with secondary H atoms, because a fast-mode shock is not just disappearing when  $B_\infty$  reaches some threshold value. It is eroding, its strength decreasing until no shock is observed.

The objective of this paper is to investigate the structure of the LISM region perturbed by the presence of the heliosphere as a function of LISM parameters. In particular, we determine the width of the LISM region perturbed by the heliosphere and the contribution of a shocked transition to the overall change of LISM properties across this region. In addition, we will consider some issues related to the formation of a boundary layer in the LISM plasma near the HP, development of instabilities and magnetic reconnection, and the HMF distribution in the presence of the heliospheric current sheet (HCS). Different problems require different models for their solution. For this reason, we use an MHD-kinetic model to investigate the bow shock behavior and the distribution of quantities in the LISM flowing around the heliopause. On the other hand, a multi-fluid approach is more appropriate for modeling the HP instabilities. Comparisons between MHD-kinetic and multi-fluid models are presented by Alexashov & Izmodenov (2005), Heerikhuisen et al. (2006), Müller et al. (2008), and Pogorelov et al. (2009c).

## 2. Constraints on the LISM Properties

As discussed in the Introduction, the LISM velocity vector and temperature can be derived from the He observations in the inner heliosphere. The rest of quantities in the unperturbed LISM are not measured directly. Following Zirnstein et al. (2016), they can be chosen to satisfy a number of observational results:

1. By analyzing the Ly $\alpha$  backscattered emission in the *Solar and Heliospheric Observatory (SOHO)* solar wind anisotropy

(SWAN) experiment, Lallement et al. (2005, 2010) discovered a deflection ( $\sim 5^\circ$ ) of the neutral H atom flow in the inner heliosphere from its original direction,  $V_\infty$ . These two directions define a so-called hydrogen deflection plane (HDP). MHD plasma/kinetic neutrals simulations (Izmodenov et al. 2005a; Pogorelov et al. 2008, 2009b; Katushkina et al. 2015) showed that the average deflection occurs predominantly parallel to the *BV*-plane.

2. It is also possible to restrict LISM properties by fitting the *IBEX* ribbon of enhanced ENA flux (see Schwadron et al. 2009, where it was determined that the directions toward the ribbon strongly correlate with the lines of sight perpendicular to the ISMF lines draping around the HP). As shown by Pogorelov et al. (2010) and Heerikhuisen & Pogorelov (2011), the position of the ENA ribbon strongly depends on rotation of the *BV*-plane about the  $V_\infty$  vector. Kinetic ENA flux simulations of Heerikhuisen et al. (2010, 2014), Heerikhuisen & Pogorelov (2011), and Zirnstein et al. (2015a, 2015b, 2016) reproduced the ribbon using the *BV*-plane consistent with the HDP. It is worth noticing here that the accuracy of *SOHO* SWAN measurements allows substantial margins in the determination of the *BV*-plane (see, e.g., Pogorelov et al. 2007). It is of interest from this viewpoint that the *BV*-plane from Zirnstein et al. (2016) lies in the middle of the range derived from the HDP analysis. Astrophysical observations restricting the ISMF properties (Frisch et al. 2015) are also consistent with the above considerations. New *IBEX* results (McComas et al. 2017) also suggest secondary ENAs as accepted ribbon source.
3. One-point-per-time, in situ measurements performed in the LISM by *VI* also provide restriction on the direction and strength of  $B_\infty$ . For example, numerical simulations of Pogorelov et al. (2009b) provided  $B_\infty \cdot R = 0$  ( $R$  is a unit vector in the radial direction) directions, consistent with the *IBEX* ribbon (McComas et al. 2009). The same choice of the LISM properties also reproduced the elevation and azimuthal angles in the ISMF beyond the HP (see Pogorelov et al. 2013c; Borovikov & Pogorelov 2014). Simulations presented in Zirnstein et al. (2016) are also restricted by the HP position and magnetic field angles observed by *VI*. It is certainly possible (see, e.g., Pogorelov et al. 2015) to shift the HP position to 122 au, where the HP was crossed by *VI* (Gurnett et al. 2013). However, the TS position in the *VI* direction becomes substantially smaller (by  $\sim 20$  au) than at the time of crossing. This should not be discouraging, since there is no information about the TS position after *Voyagers* crossed it. Numerical simulations based on *Ulysses* observations (Pogorelov et al. 2013c) indeed show that the TS was moving inward between 2004 and 2010. A decrease in the SW ram pressure from one solar cycle to another could contribute to the HP shift inward by a few au. As shown in Malama et al. (2006) and Pogorelov et al. (2016), the IHS width also decreases when PUIs are treated as a separate plasma component.
4. The H density at the TS derived from PUI measurements (Bzowski et al. 2009) can also be used to constrain the models.
5. Modeled anisotropy in the 1–10 TeV galactic cosmic ray (GCR) flux and its comparison with multiple air shower observations can also improve our knowledge of the

LISM (Schwadron et al. 2014; Zhang et al. 2014; Zhang & Pogorelov 2016).

### 3. Bow Wave and Heliospheric Boundary Layer

McComas et al. (2012) and Zank et al. (2013) investigated conditions to be satisfied for the bow shock to exist. However, a definitive answer to this question depends on the details of the global SW–LISM simulation and is not readily available from a direct analysis of the LISM properties far away from the HP. The LISM near the HP is a weakly collisional medium (the mean free path with respect to Coulomb collisions is about 1 au; Baranov & Ruderman 2013), so the bow shock, if it exists, is rather well-described by ideal MHD equations, which have the  $t$ -hyperbolic type. The source terms in these equations are due to charge exchange and therefore contain no delta-functions. As a result, the Hugoniot-type boundary conditions at a bow shock cannot be modified by such source terms. Thus, the only “shock structure” to be expected is of numerical origin. However, charge exchange modifies plasma and magnetic field both in front and behind the shock in a way unknown before the problem of the SW–LISM interaction is solved as a whole. It has been shown in the gas dynamic plasma ( $\mathbf{B} = 0$ )/kinetic neutrals simulations of Izmodenov (2000), the increase in the LISM neutral H density results in a weaker bow shock. This conclusion holds in the presence of ISMF.

Figure 2 shows the distributions of the plasma density and fast magnetosonic Mach number  $M_f = v/a_f$  along the  $x$ -axis behind the heliopause. Figure 3 shows the plasma density distributions for the same set of parameters in the meridional plane. The LISM parameters are taken from our previous simulation in Zirnstein et al. (2016), and are summarized in Table 1. For convenience, the  $\mathbf{V}_\infty$  and  $\mathbf{B}_\infty$  directions are also given in the J2000 ecliptic coordinates (Table 2). The SW properties are somewhat different from Zirnstein et al. (2016), being closer to *OMNI* data averaged over a substantial period of time (2120 days starting between 2010 DOY 1 and 2015 DOY 294) to obtain a spherically symmetric distribution at 1 au: the plasma density is  $5.924 \text{ cm}^{-3}$ , velocity  $409.8 \text{ km s}^{-1}$ , temperature  $82,336 \text{ K}$ , and radial HMF component  $39 \mu\text{G}$ .

It is clear from this figure that the LISM properties are substantially modified by charge exchange, the changes being stronger behind the fast magnetosonic shocks seen in Figures 2 (a)–(b). This is not surprising since (1) the density of secondary neutral atoms affecting the LISM ions decreases with heliocentric distance and (2) the LISM plasma density increases as it approaches the heliospheric boundary layer (HBL) on the interstellar side of the HP. It can be seen from Figure 2(c) that the shocked transition essentially disappears already at  $B_\infty = 2.75 \mu\text{G}$ ;  $M_f \approx 1.02$  ahead of it. For  $B_\infty = 3 \mu\text{G}$ ,  $M_f$  becomes smaller than 1 smoothly. Further increase in  $B_\infty$  makes the density variation from the unperturbed LISM to the HP weaker, but wider. This effect is well-known (see, e.g., Izmodenov et al. 2005a; Pogorelov et al. 2006; Borovikov et al. 2008a; Zank et al. 2010; Heerikhuisen et al. 2015). However, the solutions presented here are for the first time obtained using adaptive mesh refinement (AMR) in the OHS region (see the patch edges in Figure 2(a)), which made it possible to identify shocks inside the OHS plasma and the HBL near the HP. In some of presented simulations, such shocks are

situated inside regions of substantial variation of the LISM properties. From this viewpoint, the OHS itself can be called a “bow wave,” which forms in front of the HP due to the SW–LISM collision. This bow wave can either have a shock inside it or not, depending on the full set of SW and LISM parameters. The presence of a shocked transition inside the bow wave clearly is not determined by the condition  $M_f > 1$  in the unperturbed LISM plasma. To illustrate the spatial extent of the bow wave, in Figure 3, we show the plasma density distributions in the meridional plane for all simulations described in Table 1.

Our simulations also make it possible to understand the nature of the “boundary layer.” This layer reveals itself as a plasma density decrease in front of the HP. In previous simulations, numerical smearing of the HP made it difficult to distinguish the density increase from the solar side to the LISM across the HP itself and the density increase following it. Boundary layers are formed also upstream of the Earth’s magnetopause (Zwan & Wolf 1976), where they are called the plasma depletion layers (PDLs). Following Lees (1964) and Alksne (1967), it was shown that a PDL on the surface of the magnetosphere creates magnetic stress that affects the plasma flow. The width of such depletion layer was estimated to be about 700–1300 km for the Earth magnetosphere at  $10 R_E$  for the SW Alfvén number  $M_A = 8$  and rapidly decreasing as  $M_A$  increases. When simplistically scaled to the size of the outer heliosphere, a depletion layer at the HP would be 1%–2% of the heliocentric distance of the latter, which gives us about 1.25–2.5 au. The ions of the terrestrial magnetosheath are typically observed to have bi-Maxwellian velocity distributions with  $T_\perp/T_\parallel > 1$ , where the superscripts  $\perp$  and  $\parallel$  denote directions perpendicular and parallel to the background magnetic field. Anderson & Fuselier (1993) showed that the temperature anisotropy may be important for the PDL formation because it can launch an electromagnetic ion cyclotron instability, which makes scattered ions propagate along the magnetic field and leave the draping region. In the more recent analysis of Fuselier & Cairns (2013), the PDL width is in the range 1–5 au, which emphasizes the necessity to incorporate microphysical processes of the magnetic field draping/depletion layer formation into the PDL analysis (see also Gary et al. 1994; Denton & Lyon 1996). It is interesting to notice, however, in this connection that an HBL exists in on the LISM side of the HP in simulations without magnetic field (Baranov & Malama 1993), which means that charge exchange affects them somehow. To separate the density decrease from the LISM side to the SW side of the HP, it is necessary either to fit the HP surface, ensuring the satisfaction of the boundary conditions suitable for tangential discontinuities in MHD, or use AMR. Izmodenov & Alexashov (2015) show that such boundary layer exists also on the SW side of the HP. It is interesting to note in this connection that Belov & Ruderman (2010) argue that the density jump across the HP may disappear at the LISM stagnation point, the density variation being smooth and occurring mostly in the boundary layers.

It is seen from Figures 2 that the LISM plasma density reaches its maximum at 50–100 au from the HP surface, which is of the order of 1–2 charge exchange free paths in the OHS. The maximum values are (1) 0.2; (2) 0.175; (3) 0.155; (4) 0.14; (5) 0.115; and (6)  $0.095 \text{ cm}^{-3}$ , respectively. Further on, the plasma density is only decreasing in the sunward direction, and the maximum gradient is at the HP surface. Since we determine the HP position exactly, by solving a level-set equation for the

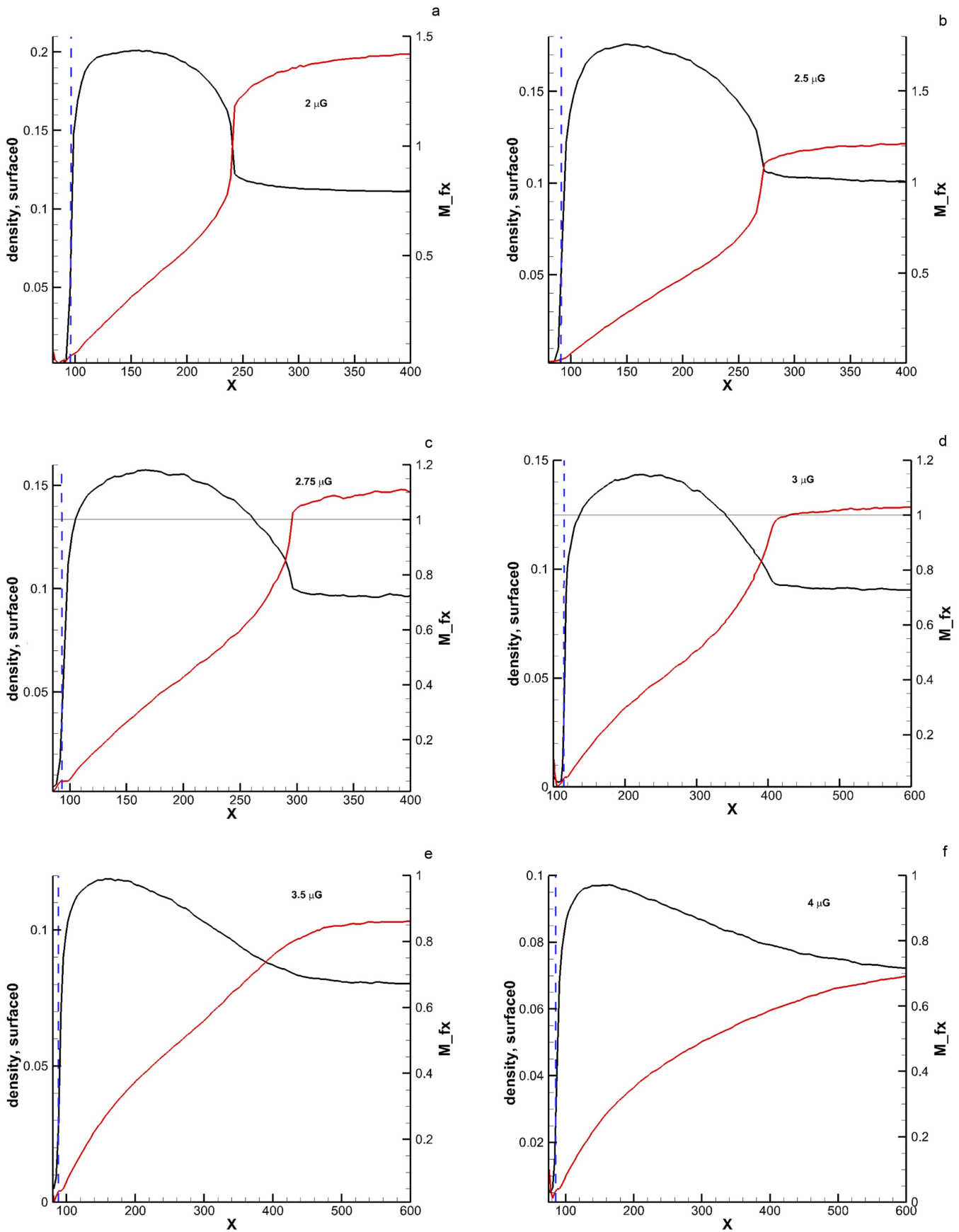


**Figure 2.** Distributions of the plasma density (black lines) and fast magnetosonic Mach number (red lines) along the  $x$ -axis in the simulations from Table 1. The vertical blue dashed lines shows the HP position.

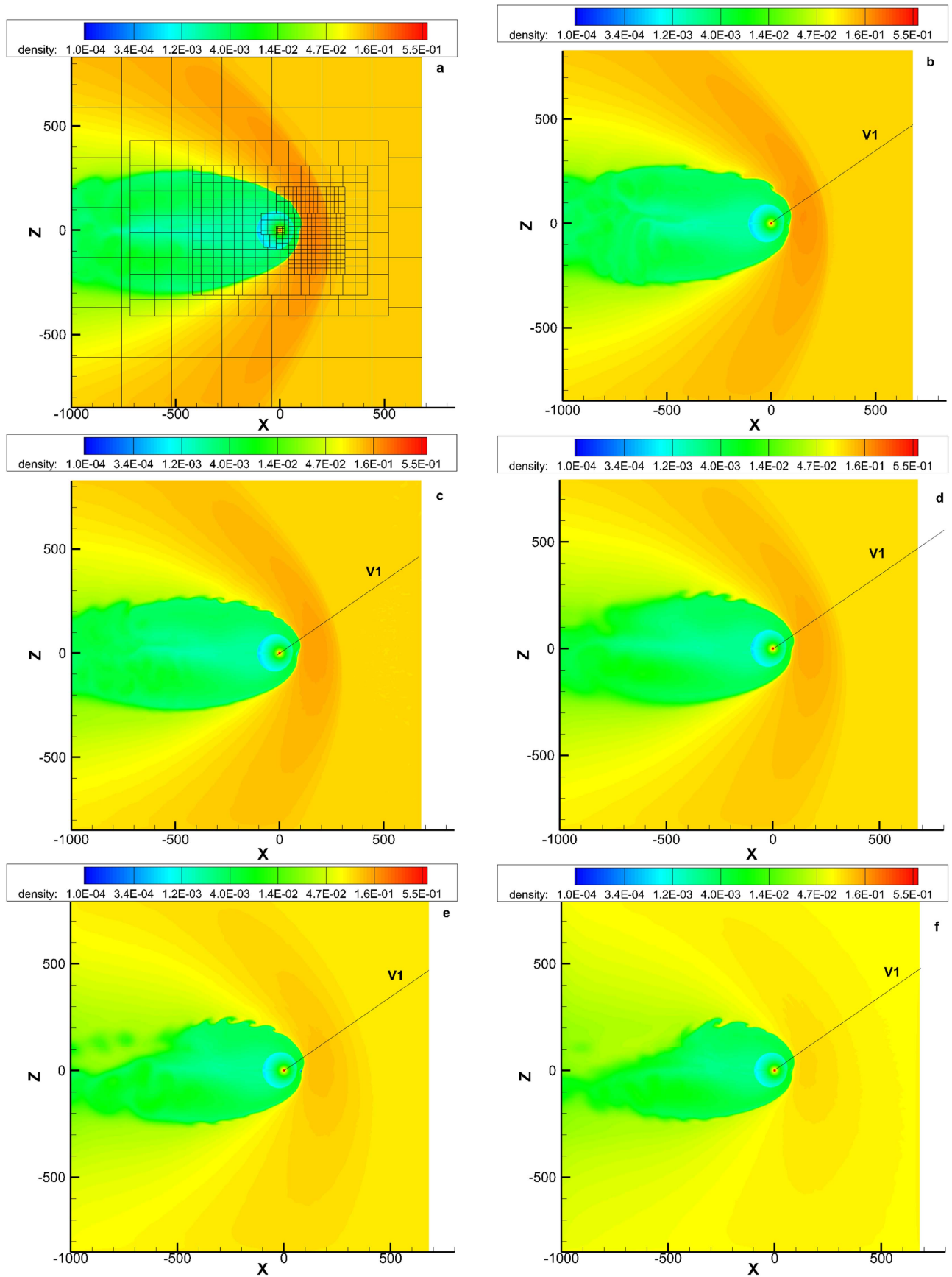


Figure 3. Distributions of the plasma density in the meridional plane for the simulations from Table 1.

**Table 1**  
Model Description for Our MHD Plasma/kinetic Neutral Atoms Simulation of the SW–LISM Interaction

Model	$n_{\infty}$ , $\text{cm}^{-3}$	$n_{\text{H}\infty}$ , $\text{cm}^{-3}$	$B_{\infty}$ , $\mu\text{G}$	$B_{\infty}/B_{\odot}$	$V_{\infty}$ , $\text{km s}^{-1}$	$V_{\infty}/V_{\odot}$	$T_{\infty}$ , K
1	0.11	0.165	2	(0.806, $-0.383, 0.452$ )	25.4	( $-0.996, 0, 0.088$ )	7500
2	0.1	0.1595	2.5	(0.760, $-0.426, 0.491$ )	25.4	( $-0.996, 0, 0.088$ )	7500
3	0.095	0.157	2.75	(0.743, $-0.441, 0.504$ )	25.4	( $-0.996, 0, 0.088$ )	7500
4	0.09	0.154	3	(0.725, $-0.455, 0.517$ )	25.4	( $-0.996, 0, 0.088$ )	7500
5	0.08	0.1495	3.5	(0.692, $-0.480, 0.539$ )	25.4	( $-0.996, 0, 0.088$ )	7500
6	0.07	0.145	4	(0.664, $-0.500, 0.556$ )	25.4	( $-0.996, 0, 0.088$ )	7500

**Table 2**

The Directions of the Unperturbed LISM Velocity and ISMF Vectors from Table 1 in the Ecliptic J2000 Coordinate System

Model	$(\lambda_{V_{\infty}}, \beta_{V_{\infty}})$ ( $^{\circ}$ )	$(\lambda_{B_{\infty}}, \beta_{B_{\infty}})$ ( $^{\circ}$ )
1	(255.7, 5.0)	(233.20, 29.86)
2	(255.7, 5.0)	(229.61, 32.83)
3	(255.7, 5.0)	(228.34, 33.81)
4	(255.7, 5.0)	(226.99, 34.82)
5	(255.7, 5.0)	(224.46, 36.61)
6	(255.7, 5.0)	(222.31, 38.02)

boundary between the SW and the LISM (Borovikov et al. 2011), we can look closer at the magnetic field and density variations in the HBL. In Figure 4, we show the magnetic field vector magnitude,  $B$ , and its elevation and azimuthal angles,  $\delta$  and  $\lambda$ , along the  $VI$  trajectory in the simulation with  $B_{\infty} = 2.75 \mu\text{G}$  from Table 1. In agreement with observations, both  $B$  and  $\lambda$  are continuous across the heliopause. The grid resolution near the HP is 1.2 au cubed. The HP position is shown with the vertical dashed line. The numerical smearing of quantities is about  $\pm 3$  au near the HP. Magnetic field strength slightly increases inside the HBL. On the other hand, the angle  $\delta$  increases to about  $28^{\circ}$ . The observed values are  $\delta = 22^{\circ} \pm 3^{\circ}$  and  $\lambda = 291^{\circ} \pm 3^{\circ}$  (Burlaga & Ness 2014a). In addition, the simulation shows a consistent undrapping of the ISMF as  $VI$  propagates deeper into the LISM. The gradients in  $\delta$  and  $\lambda$  are consistent with observations reported by Burlaga & Ness (2014b). However, these gradients become smaller if averaged from the crossing time to 2016 (Burlaga & Ness 2016). This leads us to a conclusion that time-dependent phenomena, such as described in Fermo et al. (2015), are likely to affect the undrapping.

Figure 5 shows the plasma density distribution in the meridional plane (right panel) and along the  $VI$  trajectory (left panel) in a time-dependent simulation that particularly focuses on the heliopause resolution. The LISM parameters are taken from Table 1 ( $B = 3 \mu\text{G}$ ), but a nominal (periodic with the 11 year period) solar cycle is taken into account, similarly to Pogorelov et al. (2009a) and Borovikov & Pogorelov (2014). The length scale has been decreased by a factor of 1.1 on the left panel, to ensure the HP position in the observed point. The density increase with distance from the heliopause should result in the increase of the electron oscillation plasma frequency, in accordance with  $VI$  observations with the Plasma Wave Instrument (PWS; Gurnett et al. 2015; see also Figure 6). Initially, the density increased from  $0.06 \text{ cm}^{-3}$  to  $0.08 \text{ cm}^{-3}$  from 2012 November to 2013 April–May (on the distance of  $\sim 2$  au traveled by  $VI$ ). In the figure, this distance is somewhat greater ( $\sim 2.3$  au). The next wave emission event measured by  $VI$  occurred in 2014 November and showed the density increase to about  $0.09$ – $0.11 \text{ cm}^{-3}$ . The spacecraft traveled

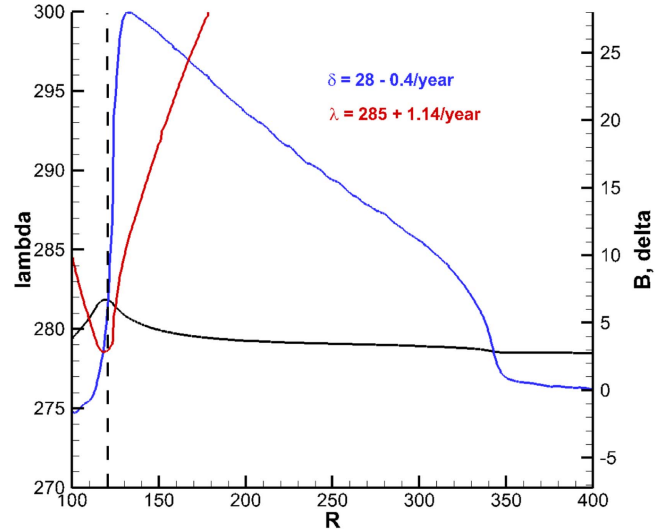


**Figure 4.** Distributions of the magnetic field vector magnitude  $B$  (black line) and its elevation (blue line) and azimuthal (red line) angles,  $\delta$  and  $\lambda$ , along the *Voyager 1* trajectory.

approximately 7 au between these events. The simulation shows the distance of about 10 au. Two more plasma oscillation events were measured by PWS: on 2015 September–November, when the density measured on Day 298, 2015 was  $0.115 \text{ cm}^{-3}$  at a distance of about 133 au from the Sun, and on Day 201, 2016, when the density was determined to be  $0.113 \text{ cm}^{-3}$  at a distance of 135.5 au. We show the latter event in Figure 5, where it occurred at  $\sim 139$  au. In addition, the measured density change between the latest two events was almost negligible, which is not seen in our simulation. These discrepancies should not be surprising because our model is not detailed enough to identify MHD shocks propagating through the OHS due to realistic time-dependent boundary conditions. The figure does show, however, the perturbations propagating through the LISM due to the solar cycle. It can be seen that there are intervals as large as 5–6 au without any density increase. The density gradient becomes smaller as  $VI$  continues to traverse the LISM, and it may take  $\sim 9$  years until it reaches the maximum density value.

#### 4. Instabilities and Magnetic Reconnection Near the Heliopause

As mentioned previously, the HP instability may be responsible for the HP “structure” observed by  $VI$  before it entered the LISM completely (Burlaga et al. 2013). The HP is also a likely venue for magnetic reconnection. It is known from both theory and simulations that the HP is unstable both at its nose and on the flanks (see Ruderman & Belov 2010; Avinash et al. 2014; Pogorelov et al. 2014, 2017, and references

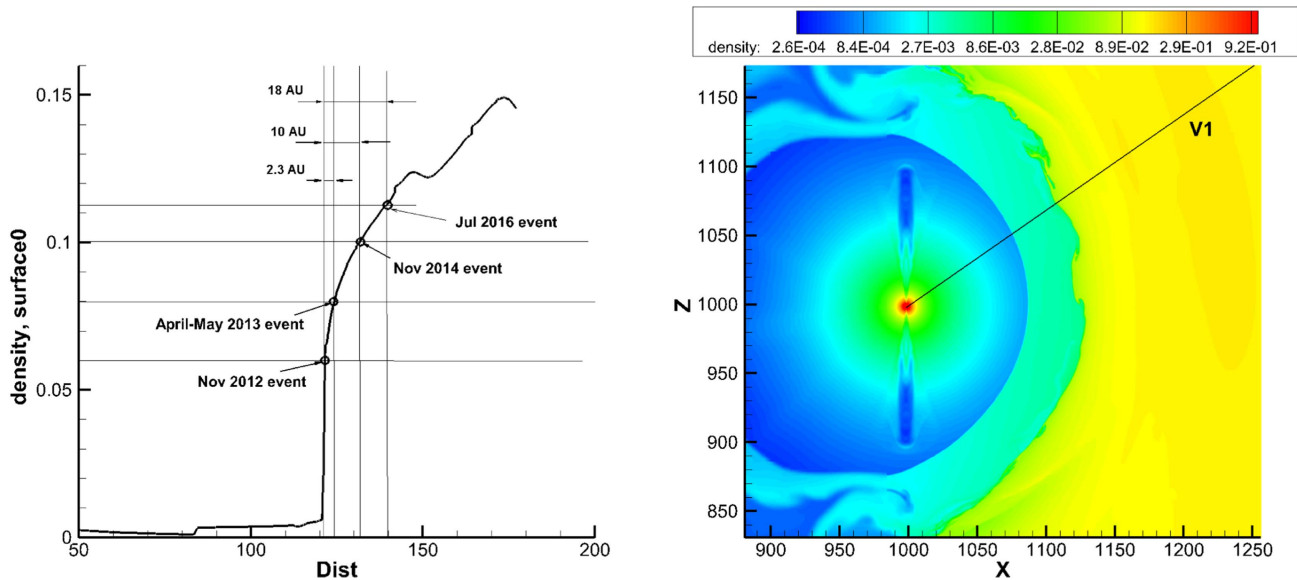


**Figure 5.** The distribution of plasma density (left panel) along the *V1* trajectory and its comparison with the plasma waves events detected by the spacecraft beyond the heliopause, and (right panel) in the meridional plane.

therein). Charge exchange between ions and neutral atoms play an important role here through the action of the source terms in the momentum and energy equations. Near the stagnation point, where the shear between the SW and LISM flow is small, charge exchange results in a sort of Rayleigh–Taylor (RT) instability (Liewer et al. 1996; Zank 1999; Florinski et al. 2005; Borovikov et al. 2008b), which is known to take place when a heavier fluid lies upon a lighter one. Farther from the stagnation point, the Kelvin–Helmholtz (KH) and other instabilities may develop (Ruderman 2015). The instabilities of the HP nose are seen only at high numerical resolution in this region ( $\sim 0.1$  au in the simulation shown below in Figure 7), which is too expensive computationally for an MHD-kinetic model. This is why, we use a multi-fluid model here with four neutral fluids involved. It is interesting to see an agreement between simulations of Borovikov et al. (2008b) and analytic analysis of Ruderman (2015) regarding the HP instability on its flanks. Both analyses demonstrate that charge exchange is primarily responsible for the flank destabilization, whereas it is further influenced by the shear flow in the HP vicinity. As shown by Borovikov & Pogorelov (2014), the HMF can partially stabilize the HP in the nose. However, previous solar cycle simulations (Pogorelov et al. 2009a, 2013c) demonstrate that the HMF indeed becomes small near the HP at certain stages of the solar cycle (see also Figure 7). This can be understood if we realize that the SW region swept by the HCS always embraces the solar equatorial plane before it reaches the TS. The SW streamlines that start in this region are directed toward a vicinity of the stagnation point on the inner side of the HP. As a result, the SW streamlines that carry magnetic field depressed by the processes occurring in the HCS-covered region of the IHS should spread over the HP surface (Pogorelov et al. 2014). Although it is shown in Borovikov & Pogorelov (2014) that the solar cycle itself is not required for the RT-instability to develop, time dependencies in the SW do affect the actual evolution of such instabilities.

The RT-instability of the HP results in a penetration of the LISM plasma into the heliosphere. This is clearly seen in Figures 7–9, which show the time evolution of the magnetic

field magnitude,  $B$ , the  $y$ -component of the magnetic field vector,  $B_y$ , and plasma density. The boundary conditions are taken from Borovikov & Pogorelov (2014), but the resolution is higher (0.22 au cubed). For better understanding of the solution behavior at *Voyager* spacecraft, the cross-cuts are made by the plane defined by the *V1* (in the northern hemisphere) and *V2* (in the southern hemisphere) trajectories. One can see that the solar cycle creates magnetic barriers of opposite polarity that propagate through the IHS toward the HP. The HMF polarity in such barriers changes every 11 years. As a barrier approaches the HP, it becomes exceedingly thinner (see Figure 8), creating the possibility of magnetic reconnection across the HP if the orientations of  $\mathbf{B}$  become suitable. The inspection of these figures demonstrates that this is especially true for the southern hemisphere, where *V2* is approaching the HP. As seen in Figures 8(d)–(e), magnetic reconnection reveals itself as a tearing mode (or plasmoid) instability. Similar features are seen in numerical modeling of magnetic reconnection during solar eruptions presented e.g., in Pontin & Wyper (2015).

It has been shown that plasmoid (tearing mode) instability of extended current sheets provides a mechanism for fast magnetic reconnection in large-scale systems. Within an MHD framework, the instability has a growth rate that increases with the Lundquist number, while its nonlinear development results in a turbulent reconnection layer and average reconnection rates that are independent of or weakly dependent on resistivity (Shibata & Tanuma 2001; Loureiro et al. 2007, 2013; Bhattacharjee et al. 2009; Uzdensky et al. 2010; Higginson et al. 2017). The conditions for such instability are satisfied for high Lundquist numbers, which can be reached by increasing the grid resolution, and large aspect ratios of the reconnecting current layers. While we do not explicitly include resistivity, magnetic diffusion proportional to  $\Delta^2$  enters our system due to discretization. Henceforth, both conditions are clearly satisfied in our simulations.

While plasmoid instability ensures that reconnection can remain fast at very large Lundquist numbers, it is by no means the only such mechanism. Simulations and theoretical



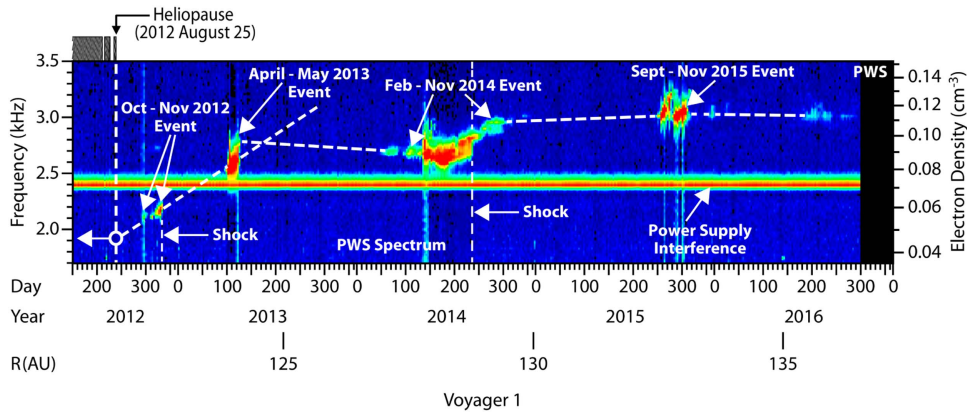


**Figure 6.** *Voyager 1* measurements of plasma oscillation frequency and electron density derived from it.

considerations demonstrate that in the presence of turbulence large-scale magnetic reconnection can proceed with large, resistivity-independent rates (e.g., Lazarian & Vishniac 1999; Eyink et al. 2011, and references therein). In fact, Beresnyak (2017) argues that the physical reason for the resistivity-independent reconnection rate is a consequence of turbulence locality, similar to models of reconnection due to ambient turbulence. Furthermore, under certain conditions, the plasmoid instability can directly transition the system to a kinetic regime where local reconnection rates again become independent of resistivity (see, e.g., Daughton et al. 2009; Daughton & Roytershteyn 2012; Ji & Daughton 2011). In addition, Zweibel et al. (2011) show that the presence of neutral atoms may modify the reconnection process. These effects, however, are beyond the scope of this paper and will be addressed elsewhere.

By tracing magnetic field lines that pass through one of the plasmoid regions shown in Figure 8, we arrive at another conclusion: the actual magnetic reconnection occurs at a distance of a few au away from this region. This conclusion has a far-reaching consequence: magnetic reconnection events have global, macroscopic features that cannot be addressed directly by kinetic simulations because of the length scale limitations intrinsic to them. A similar situation may be observed in solar flares (Liu et al. 2013), where the length of a magnetic reconnection sheet is in excess of  $10^6$  ion inertial lengths.

While more “reconnection” is seen in the southern hemisphere and at *V2*, the consequences of the HP instability are stronger at *V1*. Magnetic field distributions in Figures 7–8 demonstrate the possibility that *V1* could cross the regions belonging to the SW and LISM consecutively. This means that on the way out of the heliosphere it could be magnetically connected either to the HMF, and observe enhanced fluxes of anomalous cosmic rays (AMRs) and depressed GCR fluxes, or to the ISMF, where ACRs virtually disappear, while the GCR flux increases. This scenario requires that diffusion parallel to the magnetic field should be substantially greater than perpendicular diffusion. Luo et al. (2015) show that the abrupt increase in the GCR flux observed by *V1* when it crossed the HP is possible only if the ratio between the parallel and perpendicular diffusion coefficients exceeds  $10^4$ . Our simulations provide a plausible explanation of the changes in the ACR and GCR fluxes before *V1* entered the LISM permanently.

To supplement the results shown in Figures 7–9, we add animations of the same quantities to the online version of the paper.

## 5. Magnetic Field Dissipation in the IHS

Issues related to the magnetic field behavior at *V1* and *V2* are of great importance because both spacecraft provide us with appropriate measurements (Burlaga & Ness 2014a; Burlaga et al. 2014). In the idealized simulation considered in the previous section, the angle between the Sun’s magnetic and rotation axes is a periodic function of time. The minimum tilt of  $8^\circ$  is attained at solar activity minima, whereas the maximum of  $90^\circ$  is reached at solar activity maxima, where the magnetic dipole flips from one hemisphere to another. This is, of course, a simplification. Pogorelov et al. (2013c) considered solar cycle effects with the tilt being a function of time from WSO data. As a result, the magnetic barriers described in the previous section had a layered structure, which was due to local non-monotonicities in the tilt angle in the vicinity of the spacecraft latitude. Every non-monotonicity of this kind creates an additional current sheet.

Clearly, resolving the sectors of alternating magnetic field polarity in the IHS is impossible, even for a simplified solar cycle. This is because the sector width is proportional to the SW velocity, provided that the HCS propagates kinematically and exerts no back reaction onto the plasma surrounding it. Borovikov et al. (2011) proposed another approach to track the HCS surface. Other approaches to track the HMF polarity were used in Czechowski et al. (2010), Alexashov et al. (2016). In the approach of Borovikov et al. (2011), the HMF is assumed unipolar and a special, level-set equation is solved to propagate the HCS surface from the inner boundary toward the HP. Once the HCS surface is known, it is easy to assign proper signs to the HMF vector components at a postprocessing stage. However, this turned out to be impossible even for the level-set approach because the distances to be resolved near the HP become too small for any practically acceptable grid, so the HCS was accurately resolved only halfway from the TS to the HP. In principle, for any chosen grid resolution  $\Delta$ , this approach fails once  $\Delta/T > V$ , where  $T \approx 25$  days is the period of the Sun’s rotation. For example, for the radial SW velocity component of  $\sim 90 \text{ km s}^{-1}$ , which is currently observed at *V2*, the sector width in the solar equatorial plane is  $\sim 1.3$  au. This means that one would need at least  $\Delta \approx 0.13$  au to resolve the sector structure. Such resolutions are impossible except for over a very limited region. *Voyager 1*, on the other hand, had been observing negative radial velocity components for 2 years before it crossed the HP (Decker et al. 2012; Pogorelov et al. 2012).

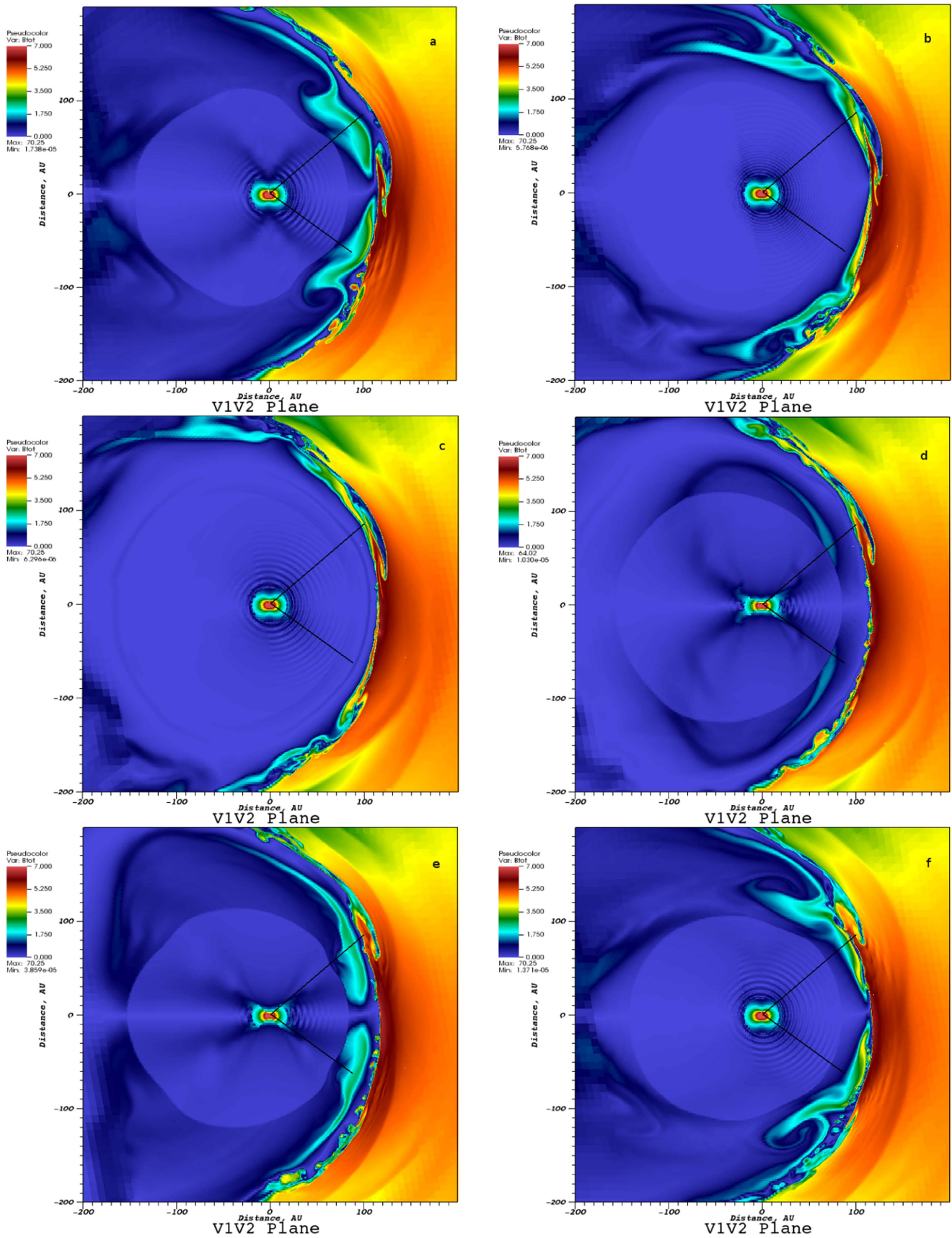


**Figure 7.** Magnetic field magnitude behavior in the plane formed by the *V1* and *V2* trajectories in the simulation that takes into account solar cycle effects. Time is increasing from the left to the right and from the top to the bottom. (An animation of this figure is available.)

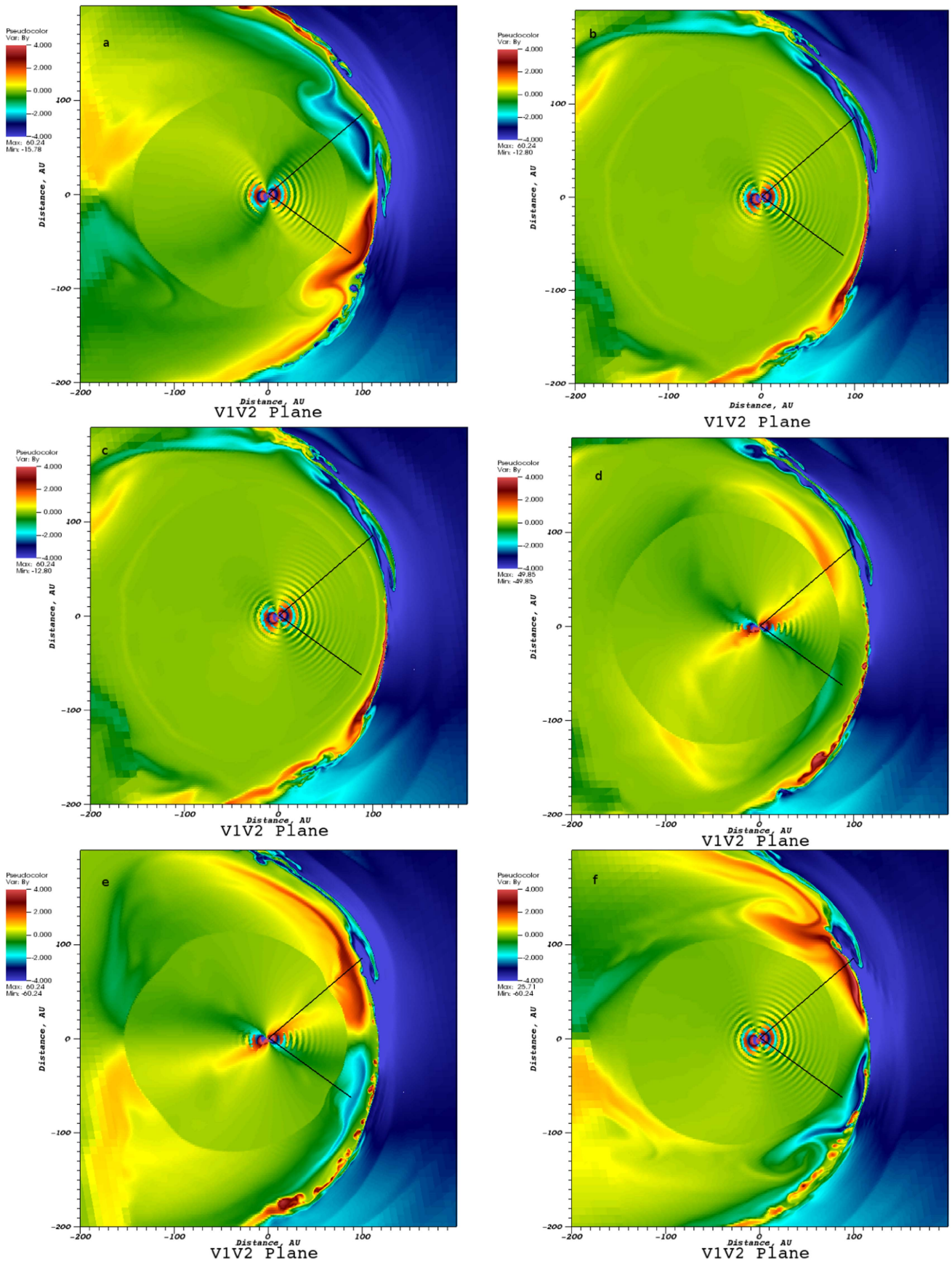


**Figure 8.** The same as in Figure 7 but for  $B_y$ .  
(An animation of this figure is available.)

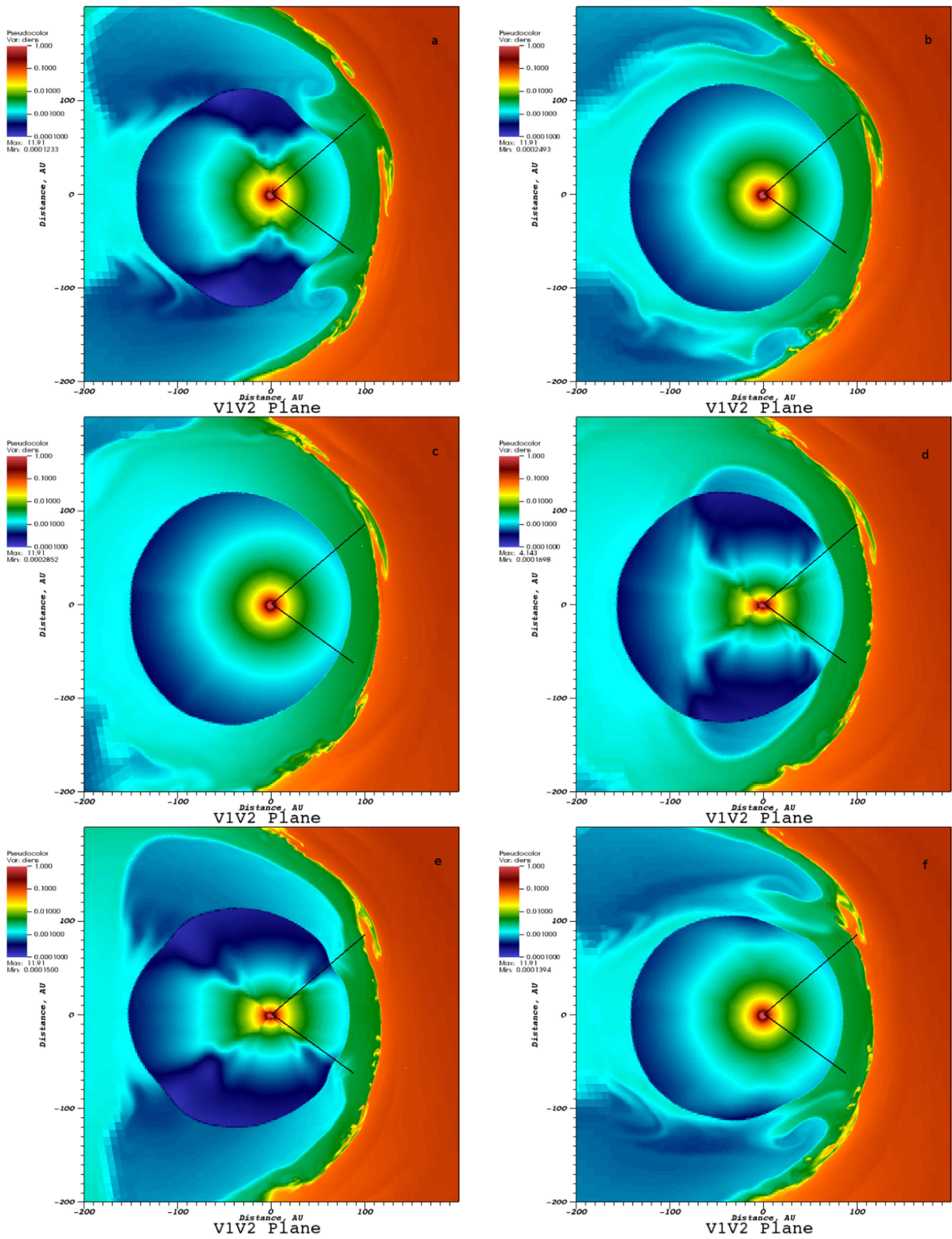


**Figure 9.** The same as in Figure 7 but for plasma density. (An animation of this figure is available.)

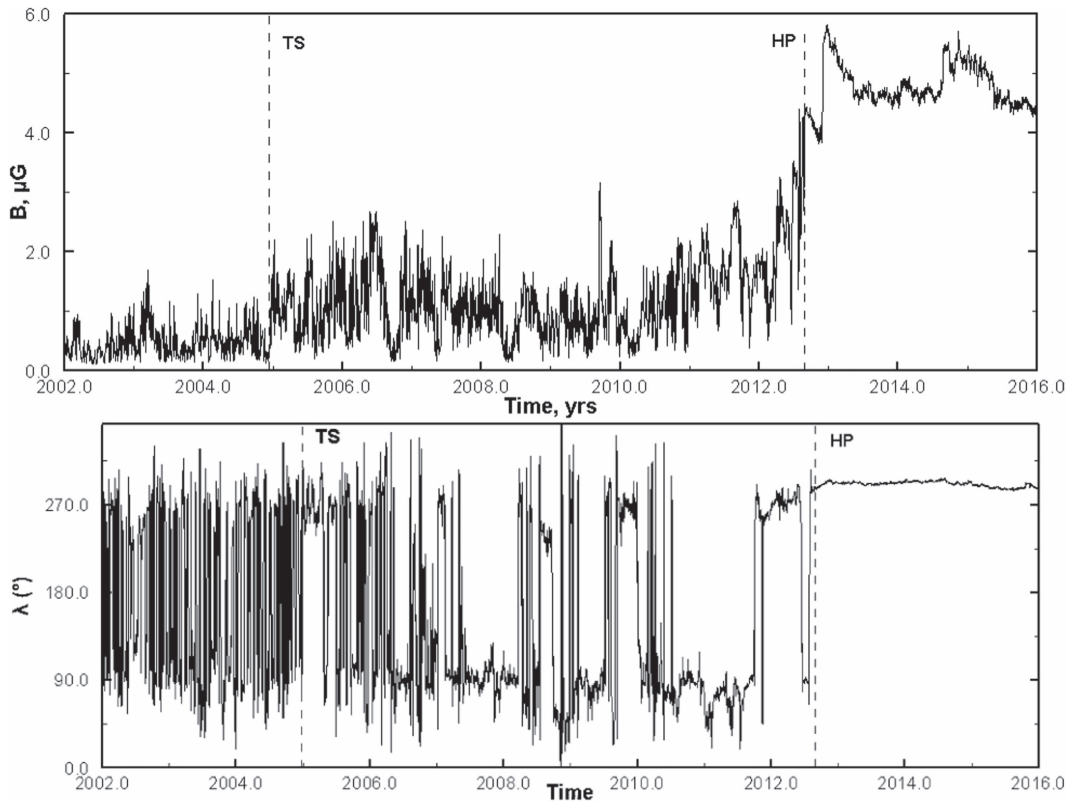


**Figure 10.** Hourly averages of the magnetic field vector magnitude and azimuthal angle along the *VI* trajectory (*Voyager* data courtesy of CohoWeb).

The sector width should be negligible in this case. Moreover, the sector width decreases to zero at the HCS tips (see Figure 14 in Pogorelov et al. 2013c), which makes attempts to resolve the traditional HCS structure questionable. We call the HCS traditional if the sector structure is entirely due to the Sun’s rotation with a fixed period.

The intervals between HCS crossings depend on the relative velocity of the SW with respect to the moving spacecraft. If  $V = 350 \text{ km s}^{-1}$  in front of the TS and becomes  $150 \text{ km s}^{-1}$  behind it, the maximum sector width was about  $0.014 \times V \text{ au}$  (i.e., 4.9 au in front of the TS and 2.1 au behind it). The velocities of *VI* and *V2* are approximately  $16.6 \text{ km s}^{-1}$  and  $14.2 \text{ km s}^{-1}$ , respectively. So *VI* should have been crossing an idealized HCS every 25.5 days before the TS and every 27 days after it, which is not the case (see Figure 10). *Voyager 2* at the current SW radial velocity of  $90 \text{ km s}^{-1}$  should cross the sectors at least every 29 days. However, observations show that it is in the unipolar region now. Clearly, the crossing intervals increase, but negligibly, which likely means that an idealized HCS does not exist.

It has been clearly established (see, e.g., Burlaga & Ness 1994) that a periodic sector structure does not exist beyond 10 or 20 au. Even at the Earth orbit, the rotating magnetic dipole model produces a two-sector quasi-periodic pattern that is seen only during the declining phase of the solar cycle, when there exist only two dominant polar coronal holes extending toward the equator. In addition, coronal mass ejections (CMEs), including magnetic clouds, disrupt the sector structure. Evolving coronal holes produce quadruple distortions of the HCS, resulting in even more complex sectors. More importantly, however, corotating and transient streams come in different sizes and shapes. They interact with each other and with CMEs to displace and modify any existing structure, while the stream structure

itself decays. These are the processes that produce the nonperiodic sector structure observed at 30 au. It is important, however, that sector boundaries are observed at large distances, at least when they are simple current sheets. This is a likely reason that Richardson et al. (2016) are able to count current sheets associated with sector boundaries.

The fluctuations in magnetic field, density, and velocity components suggest that the HCS is subject to instabilities and is likely torn into pieces as in Pogorelov et al. (2013c), where it was found that the HCS does not simply dissipate, but becomes fractured because of the tearing mode instability of the original HCS surface (see the discussion in the previous section). It should be noted, however, that the SW is turbulent both inside the TS-bounded region and in the IHS. Clearly, turbulent fluctuations should increase after the SW crosses the TS, and the HCS may be affected by this turbulence. Although we know that turbulence affects the HCS, the HP, and magnetic reconnection across them, the question is whether one should always proceed to kinetic scales to ensure fast reconnection rates (see, e.g., the particle-in-cell simulations of Drake et al. 2010 and the Hall–MHD calculations of Schreier et al. 2010). Lazarian & Vishniac (1999) identified stochastic wandering of magnetic field lines as the most critical property of MHD turbulence that permits fast reconnection. This approach has been successfully validated by Kowal et al. (2009, 2011, 2012, 2017) and Lazarian et al. (2011). It is clear that “frozen-in” magnetic field lines preclude rapid changes in magnetic topology observed at high conductivities. While microphysical plasma processes demonstrate high reconnection rates (Che et al. 2011; Daughton et al. 2011; Moser & Bellan 2012), it is an open question whether such processes can rapidly reconnect astrophysical flux structures much greater in extent than several thousand gyroradii. According to Lazarian & Vishniac (1999),

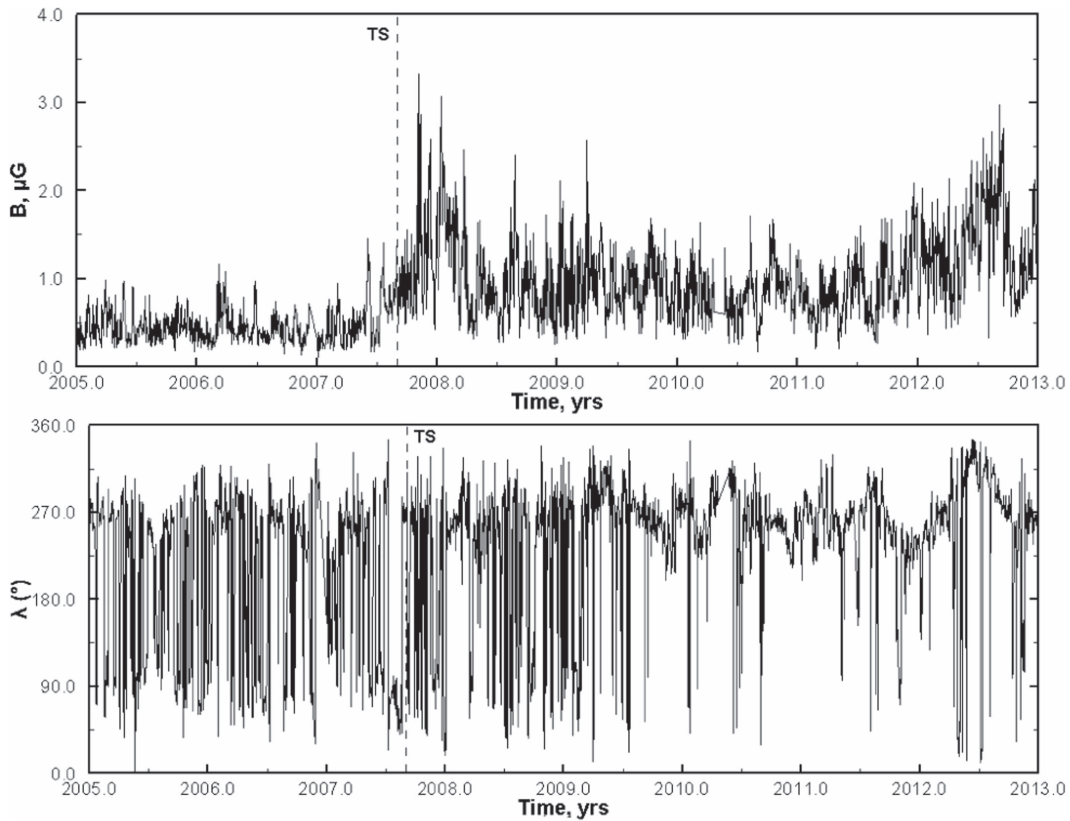


**Figure 11.** Hourly averages of the magnetic field vector magnitude and azimuthal angle along the V2 trajectory (*Voyager* data courtesy of CohoWeb).

Eyink et al. (2011, 2013), and Richardson (1926), turbulent advection brings field lines impulsively together from distances far apart to separations of the order of a few gyroradii. This scenario does not appeal to changes in the microscopic properties of plasma.

This being said, we look at the magnetic field distributions at *VI* (Figure 10) and *V2* (Figure 11) spacecraft. It is especially interesting that there is no HCS crossings at *VI* for at least 100 days after crossing the TS. The HCS is not crossed if a spacecraft moves with the velocity of the ambient SW ( $17.1 \text{ km s}^{-1}$  for *VI* and  $15.7 \text{ km s}^{-1}$  for *V2*). As shown previously, the expected “nominal” decrease in the HCS crossing time immediately beyond the TS is small. This means that either the HMF strength is too small in front of the TS, so that polarity reversals are caused not only by the HCS crossings but also by turbulent fluctuations in the SW plasma, or time-dependent phenomena make the sector structure irregular. Notice that the sectorized region of the SW plasma turns northward in the IHS, so the spacecraft should remain in the polarity-reversal region.

The sector boundaries, if not destroyed by turbulence, should be piling up in front of the HP moving inward (at *VI* before it crossed the HP) at  $20 \text{ km s}^{-1}$ , so the the number of sector crossings should have increased dramatically, but it did not. Our numerical simulations show that the absence of magnetic field polarity reversals observed by *VI* near the HP may be due to its entering a magnetic barrier. The following few polarity reversals may be caused by the complicated structure of the HP caused by its instability.

The extended periods with no polarity reversals are also seen along the *V2* trajectory. Richardson et al. (2016) have investigated the effect of the magnetic axis tilt on the number of HCS crossings and compared the observed and expected

numbers. It has been reported that the number of HCS crossings substantially decreased 2 years after *VI* and *V2* crossed the TS. However, *V2* might have entered the unipolar region at that time. It was ultimately concluded that there are indications of magnetic field dissipation possibly due to magnetic reconnection across the HCS. However, occasional deviations between the observed and expected HCS crossings are also to be expected for the reasons of stream interaction discussed previously and should not be necessarily interpreted as clear evidence for magnetic reconnection. On the other hand, as shown by Drake et al. (2017), *V2* data reveal that fluctuations in the density and magnetic field strength are anticorrelated in the sectorized regions, as expected from their magnetic reconnection modeling, but not in unipolar regions. A possible annihilation of the HMF in such regions may also be an explanation of a sharp reduction in the number of sectors, as seen from the *VI* data.

Richardson et al. (2016) assumed that the radial and latitudinal velocity components at the boundary between the unipolar and sectorized regions are determined by spacecraft measurements (i.e., are independent of latitude). However, this is not quite true. Figure 12 show that the variations in the latitudinal components can be substantial, which is not surprising because the boundary of the sectorized region should propagate from  $\sim 8^\circ$  during solar minima to  $90^\circ$  at solar maxima in 11 years. Moreover, we remember that a layer of the sectorized magnetic field never disappears on the inner side of the HP surface, at least above the equatorial plane. Only its width is a function of time. Thus a more detailed analysis of observational results may be required.

While the extent to which the HMF dissipates in the IHS remains the subject of investigation, numerical simulations allow us to find out what happens to  $B$  if the HMF is assumed

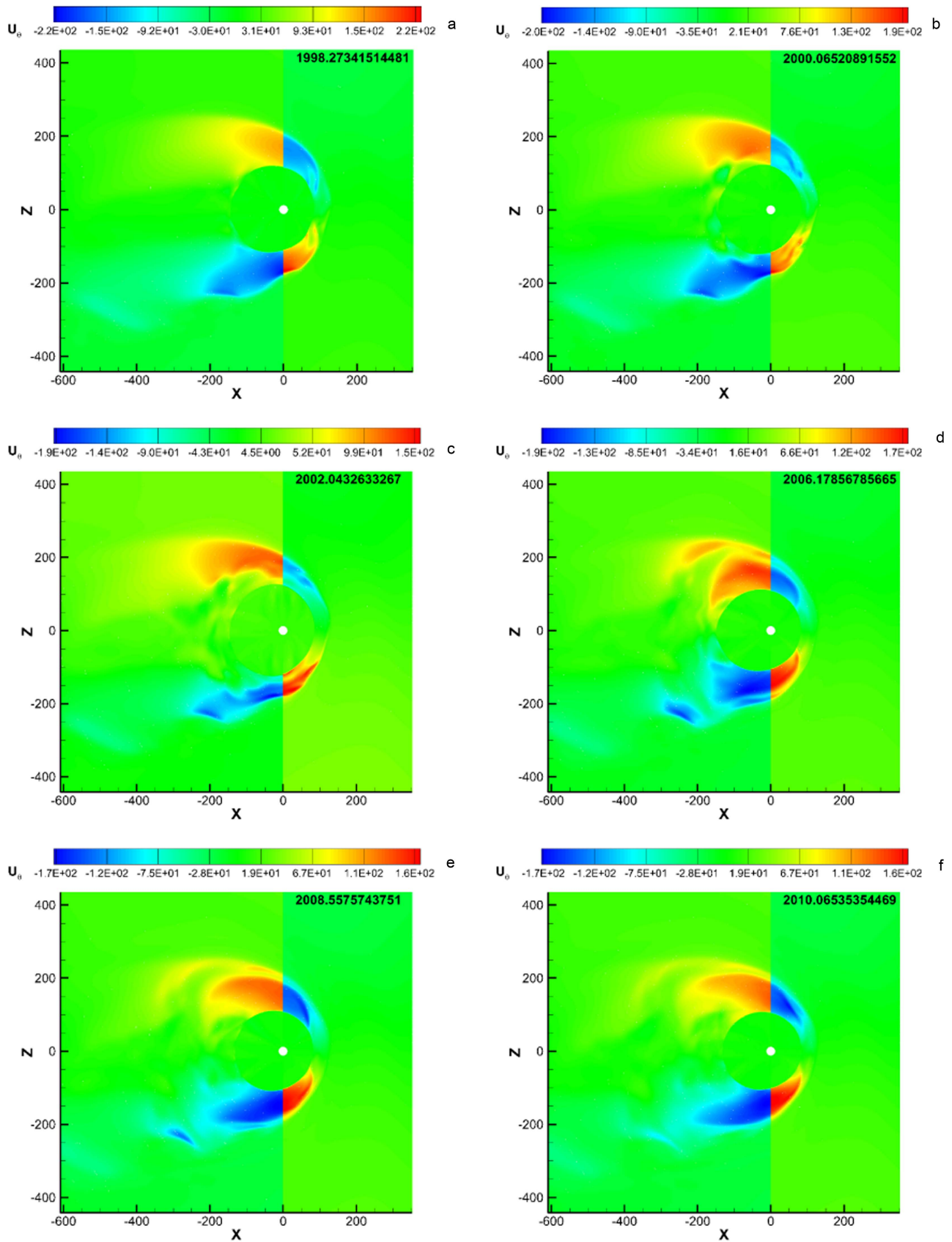


**Figure 12.** Time-dependent distributions of the latitudinal component of the velocity vector in the meridional plane in the simulation of Pogorelov et al. (2013c) demonstrate that this component strongly depends on latitude.

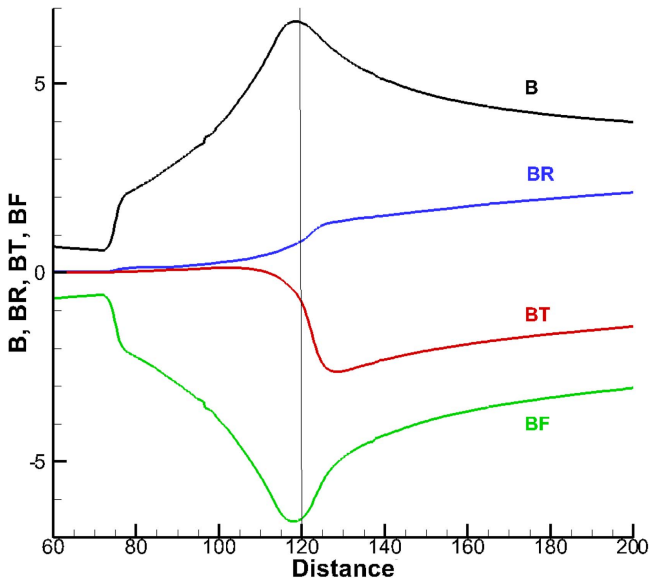


**Figure 13.** Distribution of the magnetic field strength (black line) and its radial (blue line),  $\theta$ - (red line), and  $\phi$ -components (green line) along the *VI* trajectory in an MHD-kinetic simulation where the heliospheric magnetic field is unipolar. Presented simulations demonstrate that the assumption of unipolar HMF results in a considerably overestimation of the magnetic field.

to be unipolar (see the discussions, e.g., in Pogorelov et al. 2015, 2017). Figure 13 shows the magnetic field magnitude,  $B$ , and the spherical components of  $\mathbf{B}$  along the *VI* trajectory for the simulation with  $B_\infty = 3 \mu\text{G}$  from Table 1. It is clear from this simulation that the calculated magnetic field strength is substantially overestimated (see Figure 10). This behavior of the modeled HMF at small distances beyond the TS was noticed earlier by Burlaga et al. (2009), but attributed to possible transient effects. On the other hand, based on *Ulysses* measurements, solar cycle simulations in Pogorelov et al. (2013c), which take into account the observed variations in the magnetic axis tilt with respect to the rotation axis, although not resolving the HCS, are able to reproduce *VI* observations relatively well on the average. Thus the possibility of an occasional HMF annihilation in the IHS should not be disregarded.

## 6. Conclusions

In this paper we have addressed a variety of physical phenomena related to *Voyager* observations. Some of these phenomena have clear physical explanation, whereas additional investigations, both theoretical and numerical, are necessary to describe the others. The modification of bow shocks by charge exchange between ions and neutral atoms is a well-known phenomenon, frequently referred to not only in the heliospheric bow wave context, but also in astrophysics (Chevalier & Raymond 1978; Chevalier et al. 1980; Blasi et al. 2012; Morlino et al. 2012, 2013; Morlino & Blasi 2016). Charge exchange cannot modify the Hugoniot relations at shocks (essentially the conservation laws of mass, momentum, and energy) propagating through plasma, but can substantially change the plasma properties ahead of and behind the shock. As a result, secondary H atoms of the SW origin propagate far upstream into the LISM and decrease the bow shock intensity as compared with ideal MHD flows. The structure of the bow wave in front of the heliopause is of importance for the interpretation of *IBEX* and *Voyager* observations. In addition,

Schwadron et al. (2014), Zhang et al. (2014), and Zhang & Pogorelov (2016) demonstrate that it also affects the observed anisotropy of 1–10 TeV cosmic rays. In the situation relevant to the heliospheric bow shock, the range of possible ISMF strengths,  $B_\infty$ , is such that the influence of charge exchange becomes dominant (i.e., the contribution of the shock compression to the total density [and magnetic field] enhancement on the HP surface is small). We have shown that any attempt to predict the presence of a shock in the compression region is not possible only by analyzing the properties of the LISM not affected by the presence of the HP. In the absence of such shock, the LISM interaction with the heliosphere produces a rarefaction wave propagating outward into the LISM.

High-resolution simulations show the presence of a HBL (a region of depressed plasma density and increased magnetic field strength) on the LISM side of the HP. The identification of the internal structure of such layers is a challenge for discontinuity-capturing numerical methods because of a dramatic change of plasma density across the HP. Discontinuity-fitting methods like that of Izmodenov & Baranov (2006) are more suitable for this purpose, unless substantial adaptive mesh refinement is applied. A drawback of HP-fitting methods is the difficulty to address related physical instabilities. We demonstrated that the density increase with distance from the heliopause is consistent with the plasma wave frequency observations at *VI* (Gurnett et al. 2015). It is of interest that the boundary layers seen in global simulations are not due to magnetic field effects, since they are also present in simulations without magnetic fields (Baranov & Malama 1993; Zank et al. 1996). A comparison of multi-fluid and ideal MHD simulations performed by Pogorelov & Zank (2005) suggests that the “depth” of the boundary layer increases with the LISM neutral H density. On the other hand, the width of the boundary layer seems to be comparable with the charge exchange mean free path in the LISM (40–50 au), which means that this boundary layer is somehow related to charge exchange. The relative contribution of the plasma pressure anisotropy on the HBL structure requires further investigation.

While there is little doubt that HP instabilities and magnetic reconnection are intrinsic to the heliospheric interface, it remains a challenge to relate observational data to simulation results. This is because observations are limited to one point per time, which makes it difficult to put them into the context of large-scale, 3D phenomena occurring near the HP. Indeed, the HP instability may result in substantial penetration of the LISM plasma into the SW. This, in turn, creates the possibility for a spacecraft like *VI* to cross the LISM and SW plasmas several times consecutively, which may be a reason for the changes in the observed ACR and GCR flux intensity while *VI* was crossing the HP. While this scenario still requires confirmation from a direct simulation, it is clear that a 3D, data-driven model of the SW–LISM interaction is necessary to explain the ISMF behavior along the *VI* trajectory. A few attempts to create such models have been presented recently by Fermo et al. (2015) and Kim et al. (2016, 2017). In addition to the HP instability, the simulations presented here predict that *V2* should observe more consequences of magnetic reconnection near the HP than *VI* did. This is apparently the result of the HMF–ISMF coupling at the HP. Further investigation is necessary to understand the physics of plasma wave generation and radio emission observed by *VI* in the OHS. Such investigation should also be data-driven because the ISMF undrapping observed by *VI* strongly suggest that time-dependent



phenomena are deeply involved in this process. Steady-state MHD-kinetic simulations presented here (see also Zirnstein et al. 2016) show that such undraping should be monotone.

The HCS, its behavior in the IHS, and its possible influence on the magnetic field and plasma distributions have been some of the most controversial subjects of discussion in the past few years (for a detailed analysis, see Pogorelov et al. 2017). It is clearly impossible to resolve micro-scale phenomena related to the HCS in an ideal MHD model, especially close to the HP. On the other hand, kinetic simulations of magnetic reconnection in the IHS and across the HP are too local to be able to describe the macroscopic effect of this phenomenon. While the HCS is an inherent component of magnetic field distribution in the IHS, numerical simulations allow us to perform a thought experiment where the HCS is excluded by assuming the HMF to be unipolar. As discussed previously, one may try to assign the signs to the magnetic field components *post factum*, after a unipolar simulation is finished, provided that we can track the HCS surface as a discontinuity kinematically propagating toward the HP with the SW velocity. We demonstrated here that this approach is not well-justified. If the HMF is assumed unipolar, the simulated magnetic field strength is considerably higher than it was measured by  $V1$  and  $V2$ . This is a possible explanation of the discrepancies in the simulations performed with the unipolar and dipolar HMF presented by Opher et al. (2015), Pogorelov et al. (2015, 2016), and further discussed in Pogorelov et al. (2017).

In summary, our results imply that there is some dissipation of HMF in the IHS. There are many reasons for such dissipations: (1) SW turbulence, which is especially enhanced beyond the TS; (2) magnetic reconnections; (3) kinetic and MHD instabilities; and so on. A few evidences of such dissipation are discussed in this paper (stochastic destruction of the HCS in the IHS and tearing mode instability destroying time-dependent magnetic barriers when their aspect ratios become small). Pogorelov et al. (2013b) showed that this may result in additional plasma heating and changes in the SW radial velocity component gradients. However, as far as the plasma heating is concerned, it should be clear that its analysis is impossible without proper treatment of PUIs and anomalous cosmic rays from the TS into the IHS. Pogorelov et al. (2016) demonstrated that specifically designed boundary conditions for PUIs at the TS may be able to describe the preferential heating of PUIs as compared with thermal SW ions (Zank et al. 2010). Such boundary conditions are of kinetic nature and therefore cannot be derived from any continuum mechanics approach. Approaches that are not based on the conservation-law principles and involving straightforward calculations of the PUI pressure derivatives across the TS (e.g., Usmanov et al. 2016) are mathematically flawed. Fahr & Siewert (2013; see also references therein) proposed a number of theoretical approaches to derive the previously mentioned boundary conditions. Local particle simulations may also serve as tools to help derive the boundary conditions that would be able to reproduce the ion acceleration at any point of the TS. The ion distribution function in the shock vicinity is highly anisotropic, which makes continuum mechanics approaches not applicable. We also note a recently proposed generalized system of such equations that takes into account dissipative effects and heat flux terms (Zank et al. 2014), but not taking into account possible reflection of PUIs and their further acceleration at the TS.

This work was supported NASA grants NNX14AJ53G, NNX14AF43G, NNX15AN72G, and NNX16AG83G. The work done in the University of Iowa was supported by NASA through Contract 1279980 with the Jet Propulsion Laboratory. This work was also partially supported by the *IBEX* mission as a part of NASA's Explorer program. We acknowledge NSF PRAC award ACI-1144120 and related computer resources from the Blue Waters sustained-petascale computing project. Super-computer time allocations were also provided on SGI Pleiades by NASA High-End Computing Program award SMD-16-7570 and Stamped by NSF XSEDE project MCA07S033.

The authors are grateful to G. P. Zank for stimulating discussions.

## ORCID iDs

N. V. Pogorelov  <https://orcid.org/0000-0002-6409-2392>  
L. F. Burlaga  <https://orcid.org/0000-0002-5569-1553>  
D. A. Gurnett  <https://orcid.org/0000-0003-2403-0282>

## References

- Alexashov, D., & Izmodenov, V. 2005, *A&A*, **439**, 1171  
Alexashov, D. B., Katushkina, O. A., Izmodenov, V. V., & Akaev, P. S. 2016, *MNRAS*, **458**, 2553  
Alksne, A. Y. 1967, *P&SS*, **15**, 239  
Anderson, B. J., & Fuselier, S. A. 1993, *JGR*, **98**, 1461  
Avinash, K., Zank, G. P., Dasgupta, B., & Bhadoria, S. 2014, *ApJ*, **791**, 102  
Baranov, V. B., & Malama, Y. G. 1993, *JGR*, **98**, 15157  
Baranov, V. B., & Ruderman, M. S. 2013, *MNRAS*, **434**, 3202  
Belov, N. A., & Ruderman, M. S. 2010, *MNRAS*, **401**, 607  
Beresnyak, A. 2017, *ApJ*, **834**, 47  
Bhattacharjee, A., Huang, Y., Yang, H., & Rogers, B. 2009, *PhPl*, **16**, 112102  
Blasi, P., Morlino, G., Bandiera, R., Amato, E., & Caprioli, D. 2012, *ApJ*, **755**, 121  
Blum, P. W., & Fahr, H. J. 1969, *Natur*, **223**, 936  
Borovikov, S. N., Heerikhuisen, J., Pogorelov, N. V., Kryukov, I. A., & Zank, G. P. 2008a, in ASP Conf. Ser. 385, Int. Conf. of Numerical Modeling of Space Plasma Flows (ASTRONUM 2007), ed. N. V. Pogorelov, E. Audit, & G. P. Zank (San Francisco, CA: ASP), 197  
Borovikov, S. N., & Pogorelov, N. V. 2014, *ApJL*, **783**, L16  
Borovikov, S. N., Pogorelov, N. V., Burlaga, L. F., & Richardson, J. D. 2011, *ApJL*, **728**, L21  
Borovikov, S. N., Pogorelov, N. V., Zank, G. P., & Kryukov, I. A. 2008b, *ApJ*, **682**, 1404  
Burlaga, L. F., & Ness, N. F. 1994, *JGR*, **99**, 19341  
Burlaga, L. F., & Ness, N. F. 2014a, *ApJ*, **784**, 146  
Burlaga, L. F., & Ness, N. F. 2014b, *ApJL*, **795**, L19  
Burlaga, L. F., & Ness, N. F. 2016, *ApJ*, **829**, 134  
Burlaga, L. F., Ness, N. F., Acuña, M. H., Wang, Y.-M., & Sheely, N. R., Jr. 2009, *JGRA*, **114**, A06106  
Burlaga, L. F., Ness, N. F., & Richardson, J. D. 2014, *JGRA*, **119**, 6062  
Burlaga, L. F., Ness, N. F., & Stone, E. C. 2013, *Sci*, **341**, 147  
Bzowski, M., Möbius, E., Tamopolski, S., Izmodenov, V., & Gloeckler, G. 2009, *SSRv*, **143**, 177  
Bzowski, M., Swaczyna, P., Kubiak, M. A., et al. 2015, *ApJS*, **220**, 28  
Cairns, I. H., & Zank, G. P. 2002, *GeoRL*, **29**, 1143  
Chalov, S. V., Alexashov, D. B., McComas, D., et al. 2010, *ApJL*, **716**, L99  
Che, H., Drake, J. F., & Swisdak, M. A. 2011, *Natur*, **474**, 184  
Chevalier, R. A., Kirshner, R. P., & Raymond, J. C. 1980, *ApJ*, **235**, 186  
Chevalier, R. A., & Raymond, J. C. 1978, *ApJL*, **225**, L27  
Czechowski, A., Strumik, M., Grygorczuk, J., et al. 2010, *A&A*, **516**, A17  
Daughton, W., & Roytershteyn, V. 2012, *SSRv*, **172**, 271  
Daughton, W., Roytershteyn, V., Albright, B. J., et al. 2009, *PhRvL*, **103**, 065004  
Daughton, W., Roytershteyn, V., Karimabadi, H., et al. 2011, *NatPh*, **7**, 539  
Decker, R. B., Krimigis, S. M., Roelof, E. C., & Hill, M. E. 2012, *Natur*, **489**, 124  
Denton, R. E., & Lyon, J. G. 1996, *GeoRL*, **23**, 2891  
Drake, J. F., Opher, M., Swisdak, M., & Chamoun, J. N. 2010, *ApJ*, **709**, 963  
Drake, J. F., Swisdak, M., Opher, M., & Richardson, J. D. 2017, *ApJ*, **837**, 159  
Eyink, G., Vishniac, E., Lalescu, C., et al. 2013, *Natur*, **497**, 466

- Eyink, G. L., Lazarian, A., & Vishniac, E. T. 2011, *ApJ*, **743**, 51
- Fahr, H. J., Kausch, T., & Scherer, H. 2000, *A&A*, **357**, 268
- Fahr, H. J., & Siewert, M. 2013, *A&A*, **558**, A41
- Fermo, R. L., Pogorelov, N. V., & Burlaga, L. F. 2015, *J. Phys. Conf. Ser.*, **642**, 012008
- Florinski, V., Pogorelov, N. V., Zank, G. P., Wood, B. E., & Cox, D. P. 2004, *ApJ*, **604**, 700
- Florinski, V., Zank, G. P., & Pogorelov, N. V. 2005, *JGRA*, **110**, A07104
- Frisch, P. C., Berdyugin, A., Funsten, H. O., et al. 2015, *J. Phys. Conf. Ser.*, **577**, 012010
- Frisch, P. C., Heerikhuisen, J., Pogorelov, N. V., et al. 2010, *ApJ*, **719**, 1984
- Fuselier, S. A., & Cairns, I. H. 2013, *ApJ*, **771**, 83
- Gary, S. P., Anderson, B. J., Denton, R. E., Fuselier, S. A., & McKean, M. E. 1994, *PhPI*, **1**, 1676
- Giacalone, J., & Jokipii, J. R. 2015, *ApJL*, **812**, L9
- Gruntman, M. A. 1982, *SvAL*, **8**, 24
- Gurnett, D. A., Kurth, W. S., Allendorf, S. C., & Poynter, R. L. 1993, *Sci*, **262**, 199
- Gurnett, D. A., Kurth, W. S., Burlaga, L. F., & Ness, N. F. 2013, *Sci*, **341**, 1489
- Gurnett, D. A., Kurth, W. S., Cairns, I. H., & Mitchell, J. 2006, in AIP Conf. Proc. 858, *Physics of the Inner Heliosheath: Voyager Observations, Theory, and Future Prospects*, ed. J. Heerikhuisen et al. (Melville, NY: AIP), 129
- Gurnett, D. A., Kurth, W. S., Stone, E. C., et al. 2015, *ApJ*, **809**, 121
- Heerikhuisen, J., Florinski, V., & Zank, G. P. 2006, *JGRA*, **111**, A06110
- Heerikhuisen, J., & Pogorelov, N. V. 2011, *ApJ*, **738**, 29
- Heerikhuisen, J., Pogorelov, N. V., Zank, G. P., et al. 2010, *ApJL*, **708**, L126
- Heerikhuisen, J., Zirnstein, E., & Pogorelov, N. 2015, *JGRA*, **120**, 1516
- Heerikhuisen, J., Zirnstein, E. J., Funsten, H. O., Pogorelov, N. V., & Zank, G. P. 2014, *ApJ*, **784**, 73
- Higginson, A. K., Antiochos, S. K., DeVore, C. R., Wyper, P. F., & Zurbuchen, T. H. 2017, *ApJ*, **837**, 113
- Holzer, T. E. 1977, *RvGSP*, **15**, 467
- Isenberg, P. A. 2014, *ApJ*, **787**, 6
- Izmodenov, V., Alexashov, D., & Myasnikov, A. 2005a, *A&A*, **437**, L35
- Izmodenov, V., Malama, Y., & Ruderman, M. S. 2005b, *A&A*, **429**, 1069
- Izmodenov, V. V. 2000, *Ap&SS*, **274**, 55
- Izmodenov, V. V., & Alexashov, D. B. 2003, *AstL*, **29**, 58
- Izmodenov, V. V., & Alexashov, D. B. 2015, *ApJS*, **220**, 32
- Izmodenov, V. V., & Baranov, V. B. 2006, *ISSIR*, **5**, 67
- Ji, H., & Daughton, W. 2011, *PhPI*, **18**, 111207
- Katushkina, O. A., Izmodenov, V. V., & Alexashov, D. B. 2015, *MNRAS*, **446**, 2929
- Kim, T. K., Pogorelov, N. V., & Burlaga, L. F. 2017, *ApJL*, **843**, L32
- Kim, T. K., Pogorelov, N. V., Zank, G. P., Elliott, H. A., & McComas, D. J. 2016, *ApJ*, **832**, 72
- Kowal, G., de Gouveia Dal Pino, E. M., & Lazarian, A. 2011, *ApJ*, **735**, 102
- Kowal, G., Falceta-Gonçalves, D. A., Lazarian, A., & Vishniac, E. T. 2017, *ApJ*, **838**, 91
- Kowal, G., Lazarian, A., Vishniac, E. T., & Otmianowska-Mazur, K. 2009, *ApJ*, **700**, 63
- Kowal, G., Lazarian, A., Vishniac, E. T., & Otmianowska-Mazur, K. 2012, *NPGeo*, **19**, 297
- Lallement, R., Quémerais, E., Bertaux, J.-L., et al. 2005, *Sci*, **307**, 1447
- Lallement, R., Quémerais, E., Koutroumpa, D., et al. 2010, in AIP Conf. Proc. 1216, *Twelfth International Solar Wind Conf.*, ed. M. Maksimovic et al. (New York: AIP), 555
- Lazarian, A., Kowal, G., Vishniac, E., & de Gouveia Dal Pino, E. 2011, *P&SS*, **59**, 537
- Lazarian, A., & Vishniac, E. T. 1999, *ApJ*, **517**, 700
- Lees, L. 1964, *AIAA J.*, **2**, 1576
- Liewer, P. C., Karmesin, S. R., & Brackbill, J. U. 1996, *JGR*, **101**, 17119
- Liu, W., Chen, Q., & Petrosian, V. 2013, *ApJ*, **767**, 168
- Loureiro, N. F., Schekochihin, A. A., & Cowley, S. C. 2007, *PhPI*, **14**, 100703
- Loureiro, N. F., Schekochihin, A. A., & Uzdensky, D. A. 2013, *PhRvE*, **87**, 013102
- Luo, X., Zhang, M., Potgieter, M., Feng, X., & Pogorelov, N. V. 2015, *ApJ*, **808**, 82
- Malama, Y. G., Izmodenov, V. V., & Chalov, S. V. 2006, *A&A*, **445**, 693
- McComas, D. J., Alexashov, D., Bzowski, M., et al. 2012, *Sci*, **336**, 1291
- McComas, D. J., Allegrini, F., Bochsler, P., et al. 2009, *Sci*, **326**, 959
- McComas, D. J., Bzowski, M., Frisch, P., et al. 2015, *ApJ*, **801**, 28
- McComas, D. J., Zirnstein, E. J., Bzowski, M., et al. 2017, *ApJS*, **229**, 41
- Mitchell, J. J., Cairns, I. H., & Heerikhuisen, J. 2009, *GeoRL*, **36**, L12109
- Morlino, G., Bandiera, R., Blasi, P., & Amato, E. 2012, *ApJ*, **760**, 137
- Morlino, G., & Blasi, P. 2016, *A&A*, **589**, A7
- Morlino, G., Blasi, P., Bandiera, R., & Amato, E. 2013, *A&A*, **558**, A25
- Moser, A. L., & Bellan, P. M. 2012, *Natur*, **482**, 379
- Müller, H.-R., Florinski, V., Heerikhuisen, J., et al. 2008, *A&A*, **491**, 43
- Opher, M., Drake, J. F., Zieger, B., & Gombosi, T. I. 2015, *ApJ*, **800**, 28
- Pauls, H. L., Zank, G. P., & Williams, L. L. 1995, *JGR*, **100**, 21595
- Pogorelov, N. V., Bedford, M. C., Kryukov, I. A., & Zank, G. P. 2016, *J. Phys. Conf. Ser.*, **767**, 012020
- Pogorelov, N. V., Borovikov, S. N., Bedford, M. C., et al. 2013a, in ASP Conf. Ser. 474, *7th Int. Conf. of Numerical Modeling of Space Plasma Flows (ASTRONUM 2012)*, ed. N. V. Pogorelov, E. Audit, & G. P. Zank (San Francisco, CA: ASP), 165
- Pogorelov, N. V., Borovikov, S. N., Burlaga, L. F., et al. 2013b, in AIP Conf. Proc. 1539, *Solar Wind 13*, ed. G. P. Zank et al. (Melville, NY: AIP), 352
- Pogorelov, N. V., Borovikov, S. N., Heerikhuisen, J., Kim, T. K., & Zank, G. P. 2014, in ASP Conf. Ser. 488, *8th Int. Conf. of Numerical Modeling of Space Plasma Flows (ASTRONUM 2013)*, ed. N. V. Pogorelov, E. Audit, & G. P. Zank (San Francisco, CA: ASP), 167
- Pogorelov, N. V., Borovikov, S. N., Heerikhuisen, J., & Zhang, M. 2015, *ApJL*, **812**, L6
- Pogorelov, N. V., Borovikov, S. N., Zank, G. P., et al. 2012, *ApJL*, **750**, L4
- Pogorelov, N. V., Borovikov, S. N., Zank, G. P., & Ogino, T. 2009a, *ApJ*, **696**, 1478
- Pogorelov, N. V., Fichtner, H., Czechowski, A., et al. 2017, *SSRv*, doi:10.1007/s11214-017-0354-8
- Pogorelov, N. V., Heerikhuisen, J., Borovikov, S. N., et al. 2010, in AIP Conf. Proc. 1302, *Pickup Ions Throughout the Heliosphere and Beyond*, ed. J. A. le Roux et al. (Melville, NY: AIP), 3
- Pogorelov, N. V., Heerikhuisen, J., Mitchell, J. J., Cairns, I. H., & Zank, G. P. 2009b, *ApJL*, **695**, L31
- Pogorelov, N. V., Heerikhuisen, J., & Zank, G. P. 2008, *ApJL*, **675**, L41
- Pogorelov, N. V., Heerikhuisen, J., Zank, G. P., et al. 2011, *ApJ*, **742**, 104
- Pogorelov, N. V., Heerikhuisen, J., Zank, G. P., & Borovikov, S. N. 2009c, *SSRv*, **143**, 31
- Pogorelov, N. V., Stone, E. C., Florinski, V., & Zank, G. P. 2007, *ApJ*, **668**, 611
- Pogorelov, N. V., Suess, S. T., Borovikov, S. N., et al. 2013c, *ApJ*, **772**, 2
- Pogorelov, N. V., & Zank, G. P. 2005, *AdSpR*, **35**, 2055
- Pogorelov, N. V., Zank, G. P., & Ogino, T. 2006, *ApJ*, **644**, 1299
- Pontin, D. I., & Wyper, P. F. 2015, *ApJ*, **805**, 39
- Richardson, J. D., Burlaga, L. F., Drake, J. F., Hill, M. E., & Opher, M. 2016, *ApJ*, **831**, 115
- Richardson, L. F. 1926, *RSPSA*, **110**, 709
- Ruderman, M. S. 2015, *A&A*, **580**, A37
- Ruderman, M. S., & Belov, N. A. 2010, *J. Phys. Conf. Ser.*, **216**, 012016
- Schreier, R., Swisdak, M., Drake, J. F., & Cassak, P. A. 2010, *PhPI*, **17**, 110704
- Schwadron, N. A., Adams, F. C., Christian, E. R., et al. 2014, *Sci*, **343**, 998
- Schwadron, N. A., Bzowski, M., Crew, G. B., et al. 2009, *Sci*, **326**, 966
- Shibata, K., & Tanuma, S. 2001, *EP&S*, **53**, 473
- Sternal, O., Fichtner, H., & Scherer, K. 2008, *A&A*, **477**, 365
- Usmanov, A. V., Goldstein, M. L., & Matthaeus, W. H. 2016, *ApJ*, **820**, 17
- Uzdensky, D., Loureiro, N., & Schekochihin, A. 2010, *PhRvL*, **105**, 235002
- Wallis, M. 1971, *NPhS*, **23**, 23
- Wallis, M. K. 1975, *Natur*, **254**, 202
- Witte, M. 2004, *A&A*, **426**, 835
- Zank, G. P. 1999, in AIP Conf. Ser. 471, *The Dynamical Heliosphere*, ed. S. R. Habbal et al. (Melville, NY: AIP), 783
- Zank, G. P., Heerikhuisen, J., Pogorelov, N. V., Burrows, R., & McComas, D. J. 2010, *ApJ*, **708**, 1092
- Zank, G. P., Heerikhuisen, J., Wood, B. E., et al. 2013, *ApJ*, **763**, 20
- Zank, G. P., Hunana, P., Mostafavi, P., & Goldstein, M. L. 2014, *ApJ*, **797**, 87
- Zank, G. P., & Müller, H.-R. 2003, *JGRA*, **108**, 1240
- Zank, G. P., Pauls, H. L., Williams, L. L., & Hall, D. T. 1996, *JGRA*, **101**, 21639
- Zhang, M., & Pogorelov, N. 2016, *J. Phys. Conf. Ser.*, **767**, 012027
- Zhang, M., Zuo, P., & Pogorelov, N. 2014, *ApJ*, **790**, 5
- Zieger, B., Opher, M., Schwadron, N. A., McComas, D. J., & Tóth, G. 2013, *GeoRL*, **40**, 2923
- Zirnstein, E. J., Heerikhuisen, J., Funsten, H. O., et al. 2016, *ApJL*, **818**, L18
- Zirnstein, E. J., Heerikhuisen, J., & McComas, D. J. 2015a, *ApJL*, **804**, L22
- Zirnstein, E. J., Heerikhuisen, J., Pogorelov, N. V., McComas, D. J., & Dayeh, M. A. 2015b, *ApJ*, **804**, 5
- Zwan, B. J., & Wolf, R. A. 1976, *JGR*, **81**, 1636
- Zweibel, E. G., Lawrence, E., Yoo, J., et al. 2011, *PhPI*, **18**, 111211